NASA
Technical
Paper
2307

August 1985

Experimental Aerodynamic Heating to Simulated Space Shuttle Tiles in Laminar and Turbulent Boundary Layers With Variable Flow Angles at a Nominal Mach Number of 7

Don E. Avery

NASA

NASA Technical Paper 2307

1985

Experimental Aerodynamic Heating to Simulated Space Shuttle Tiles in Laminar and Turbulent Boundary Layers With Variable Flow Angles at a Nominal Mach Number of 7

Don E. Avery

Langley Research Center
Hampton, Virginia

NASA

National Aeronautics
and Space Administration

**Scientific and Technical
Information Branch**

Summary

The heat transfer to simulated Shuttle thermal protection system tiles was investigated experimentally by using a highly instrumented metallic thin-wall tile arranged with other metal tiles in a staggered tile array. This study extends previous efforts by including the effect of the flow angularity on localized heating in the upstream tile corner and "T" gap (an arrangement in which longitudinal gaps terminate at intersections with transverse gaps). Flow angles investigated include 0°, 15°, 30°, 45°, and 60°. Cold-wall heating-rate data for laminar and turbulent flow were obtained in the Langley 8-Foot High-Temperature Tunnel at a nominal Mach number of 7, a nominal total temperature of 3300°R, a free-stream unit Reynolds number from 3.4×10^5 to 2.2×10^6 per foot, and a free-stream dynamic pressure from 2.1 to 9.0 psia. Experimental data are presented to illustrate the effects of flow angularity and gap width on both local peak heating and overall heating loads. For the conditions of the present study, the results show that localized and total heating are sensitive to changes in flow angle only for the test conditions of turbulent boundary-layer flow with high kinetic energy and that a flow angle from 30° to 50° will minimize the local heating.

Introduction

The Space Shuttle orbiter was designed for a 100-mission life with minimal refurbishment between missions (ref. 1). In order to meet this requirement, the current Shuttle design uses several methods of thermal protection (refs. 2 and 3) to insulate the aluminum primary structure from the extremely hostile aerodynamic environment. The primary thermal protection system (TPS) is a reusable surface insulation (RSI) made up of fibrous silica-based material tiles with a high-emissivity coating.

The Shuttle RSI tiles are nominally 6 by 6 by 2.5 in. The actual thickness is varied according to the expected heat load. The outer surface of the RSI must withstand temperatures of approximately 3060°R on the bottom surface of the orbiter and maintain a primary structure temperature below 810°R during entry into the Earth's atmosphere. The RSI is bonded to a strain isolator pad that is then bonded to the primary structure of the Shuttle. The RSI tiles are applied to the surface with gaps (nominally 0.045 in.) between the tiles to accommodate thermal expansion and contraction and mechanical deflection of the underlying structure as well as to allow for thermal expansion of the tile material. The gaps between the tiles locally disrupt the external boundary layer and, therefore, increase the aerodynamic heating during entry. To reduce the heat load on the lower surface of the Shuttle, the tiles are arranged in a staggered pattern with the tile leading edges swept 45° relative to the Shuttle centerline. However, during atmospheric entry the local flow angle varies relative to the tile leading edge.

Previous aerothermal tests (refs. 4 to 10) on simulated Shuttle tiles provided a data base of localized and overall heating on the tiles. The localized heating affects the tile coating life, whereas the overall heating affects the structural integrity of both tile and primary structure. From this data base, correlations were developed for localized heating effects as influenced by boundary layer and gap geometry. More recent research described in reference 11 extended the data base for localized heating in the "T" gap region (an arrangement in which longitudinal gaps terminate at intersections with transverse gaps) with more detailed measurements. Empirical relationships, which were developed from the entire data base, successfully predicted the effects of tile geometry and of laminar- and turbulent-flow parameters on the localized heating in the "T" gap region for flow aligned at 0° relative to the longitudinal gap.

The present experimental study extends the data base further to include the effect of flow angularity on localized and overall heating in laminar and turbulent flow. Cold-wall heating rates were obtained in the Langley 8-Foot High-Temperature Tunnel (occasionally referred to herein as the 8' HTT) at a nominal Mach number of 7, a nominal total temperature of 3300°R, a free-stream unit Reynolds number from 3.4×10^5 to 2.2×10^6 per foot, and a free-stream dynamic pressure from 2.1 to 9.0 psia. When the flow angle is included as a parameter, another high localized heating region is created on a tile upstream corner in addition to the "T" gap region. The flow angles tested included 0°, 15°, 30°, 45°, and 60°. In addition, the effects of boundary-layer state, Reynolds number, and gap width on localized and overall heating were investigated. The need for detailed distributions in the localized heating regions, as well as for overall heating distributions, required the installation of a large number of thermocouples in a small thin-wall model. A new fabrication technique (ref. 12) was developed to construct a Niculoy 22[1] electrolessly plated thin-wall model instrumented with 256 one-wire thermocouples.

Symbols

B distance from tile bottom edge to tile center (fig. 11), in.

[1] Niculoy 22: Registered trademark of Shipley Company, Inc.

c_p	specific heat of Niculoy 22, Btu/lbm-°R
H	tile height, in.
L	gap length (see fig. 5), in.
M	local Mach number
P	ratio of static pressure to pitot pressure in test stream
Q	total heat load to tile, Btu/sec
$\dot{q}$	heating rate, Btu/ft^2-sec
q_∞	free-stream dynamic pressure, psia
R	local Reynolds number based on distance from leading edge of panel holder to center of instrumented tile
r	model distance from centerline of tunnel nozzle, in.
S	distance around perimeter of tile, in.
T	temperature, °R
T_R	ratio of tunnel test section to combustor stagnation temperature in test stream
$T_{t,c}$	total temperature in combustor, °R
t	time, sec
W	gap width (see fig. 5), in.
x, y, z	thermocouple coordinate system (fig. 7), in.
α	angle of attack, deg
Λ	flow angle relative to longitudinal gap, deg
ρ	density of Niculoy 22, lbm/ft^3
τ	model wall thickness, ft

Subscripts:

corr	corrected
FP	flat plate

Abbreviations:

℄	centerline
RSI	reusable surface insulation
TC	thermocouple
TPS	thermal protection system

Experimental Apparatus and Procedures

Test Facility

The Langley 8-Foot High-Temperature Tunnel (formerly the Langley 8-Foot High-Temperature Structures Tunnel; see fig. 1) is a large blowdown facility that simulates aerodynamic heating and pressure loading at a nominal Mach number of 7 at altitudes between 80 000 and 120 000 ft. The high energy needed for this simulation is obtained by burning a mixture of methane and air under pressure in the combustor and expanding the products of combustion through a conical-contoured nozzle into the free-jet test chamber. The flow enters a supersonic diffuser in which the air ejector pumps the flow through a mixing tube and exhausts the flow to the atmosphere through a subsonic diffuser. This tunnel operates at combustor total temperatures between 2400°R and 3600°R, free-stream dynamic pressures from 250 to 1800 psf, and free-stream unit Reynolds numbers per foot from 0.3×10^6. The tunnel has an 8-ft-diameter free-jet test section, and the test stream has a 4-ft-diameter core in which the test conditions are uniform. Figure 2 shows typical Mach number, temperature, and pressure distributions radially from the center of the test stream (tunnel centerline) for one test condition (total pressure in combustor of 1025 psia and $T_{t,c} = 3000$°R).

The panel holder containing the model is stored in the pod below the test stream to protect it from adverse tunnel start-up transients and acoustic loads. Once the desired flow conditions are established, the panel holder is inserted into the test stream on a hydraulically actuated elevator in approximately 1.5 sec to approximate a step heat input to the model. A panel-holder pitch system provides an angle-of-attack range from $-20°$ to $20°$. More detailed information about the 8' HTT can be found in references 13 to 15.

The panel holder (figs. 3 and 4) can accommodate test panels up to 42.5 by 60 in. (See refs. 13 and 14.) The aerodynamic surface ahead of the model consists of 1-in-thick low conductivity tiles and a 3/8-in-thick steel plate. Aerodynamic fences provide uniform two-dimensional flow over the entire aerodynamic surface. A blunt leading edge with a radius of 0.374 in. is used on the panel holder to promote a low-energy laminar boundary layer, and a blunt or sharp leading edge with a lateral row of 0.09-in-diameter spherical boundary-layer trips is used to produce a low- or high-energy turbulent boundary layer (respectively) over the aerodynamic surface of the panel holder. The designations "low- and high-energy boundary layers" used herein refer to the available energy in the boundary layer. Low-available-energy boundary

layers are created when the approaching flow field passes through a nonisentropic normal shock ahead of a blunt leading edge. High-available-energy boundary layers are created when the approaching flow passes through a nearly isentropic oblique shock attached to a sharp leading edge. The leading edge of the model was located 61.1 in. from the blunt leading edge of the panel holder and 62.7 in. from the sharp leading edge of the panel holder.

Model and Instrumentation

The model used in this study consisted of a metallic tile array to simulate the reusable surface insulation (RSI) of the thermal protection system (TPS) of the Space Shuttle. Metallic tiles were used in lieu of RSI tiles because of their ease to handle and instrument. The tile material has no effect on the cold-wall heating rates at these test conditions. The 20- by 20- by 2.5-in. tile array (fig. 5) was basically the same array as that used in reference 11, except that the 5.9- by 6.4-in. center tile was replaced with a highly instrumented tile (fig. 6) and the two stainless-steel thin-wall tiles were not used to obtain data. The remaining tiles were solid aluminum blocks and all tiles had 0.10-in. edge radii. All the tiles were bolted to a 0.13-in-thick stainless-steel plate and sealed to prevent flow under the tiles. Slotted bolt holes permitted adjustments of the tile positions to vary gap width with respect to the center tile. The gap widths W studied were 0.040, 0.070, 0.120, and 0.160 in. with longitudinal and transverse gap widths equal. The tile array was mounted in a turntable that allowed the flow angle Λ to be varied to 0°, 15°, 30°, 45°, and 60° with respect to the longitudinal gap.

Conventional fabrication techniques used for the stainless-steel thin-wall tiles in reference 11 were not employed because of the following: (1) a high concentration of instrumentation in localized heating regions, such as in the corners and edges, was desired, and (2) a uniform tile thickness along the tile corners and edges could not be achieved. Consequently, a new electrolessly plated nickel process (ref. 12) was developed to fabricate a tile with high-density instrumentation, as shown in figures 6 and 7 (rotated 90° counterclockwise relative to fig. 5). The process was an extension of techniques developed under a NASA Johnson Space Center contract (ref. 16) to fabricate a small electrolessly plated nickel model instrumented with one-wire thermocouples. The small-diameter (0.005 in.) one-wire thermocouples permitted a higher concentration of instrumentation with reduction in thermal losses through the wire than can be obtained with standard two-wire techniques.

The new fabrication technique used six steps to produce a mandrel with 256 precisely located constantan thermocouple wires protruding from the mandrel. Niculoy 22 was then electrolessly plated over the mandrel to one-half the tile thickness (0.0125 in.). The protruding thermocouple wires were clipped and polished smooth with the tile surface, and a second 0.0125-in. layer of Niculoy 22 was plated on the surface. A typical cross section of a thermocouple junction is shown in the insert of figure 7. Finally, the mandrel was melted away leaving a free-standing thin-wall shell. As seen in figure 7 and table I, the thermocouples were located on all tile surfaces with concentrations in known localized high heating zones.

Test Procedures and Conditions

The wind-tunnel equilibrium flow conditions were established and then the model, installed in the panel holder, was inserted into the test stream. The model was pitched to the desired angle of attack before insertion into the test stream. The model was exposed to the flow approximately 2 sec to avoid exceeding the 960°R temperature limit of the thin-wall tile, to minimize thermal gradients and attendant thermal stresses, and to minimize conduction errors.

A total of 26 tests were conducted; 8 were with laminar flow and 19 were with turbulent flow. Table II outlines the tunnel flow conditions, the corresponding panel holder, and the model geometry. The free-stream tunnel conditions were determined from temperatures and pressures measured in the combustor and are based on the thermal and transport properties of methane-air combustion products, as reported in reference 17 and in the panel-holder surveys of reference 14. Figure 8 shows typical Mach number profiles on the panel holder for three test conditions. Data for these profiles were obtained from a boundary-layer probe shown in figures 3 and 4, and the Mach numbers were calculated by using the Rayleigh pitot equation with ratio of specific heats for the flow media. Test 2 represents laminar-flow conditions, test 16 represents low-energy turbulent flow, and test 17 represents high-energy turbulent flow. For turbulent flow, a considerable difference in the boundary-layer Mach number exists between the low- and high-energy flows. At a distance 0.070 in. (nominal experimental gap width) above the aerodynamic surface, the Mach number for low-energy turbulent flow is 0.9 and 2.6 for high-energy turbulent flow. The calculated local Mach numbers (blunt-nose calculations use normal-shock entropy) at the edge of the boundary layer are shown by the tick marks in figure 8.

The top surface of the instrumented tile was intended to be flush mounted with the other tiles for all tests; however, a posttest check indicated that

a nominal step height of 0.035 in. was present for test 19. The effect of a step height will be reported subsequently in the "Results and Discussion" section.

Measurement Technique

Cold-wall heating-rate data were calculated from the output of 256 constantan one-wire thermocouples with an ambient reference temperature junction. The junction was located in a thermally isolated box inside the panel holder. The tile wall served as the other thermocouple wire to complete the thermocouple circuit, thereby forming a Niculoy 22/constantan thermocouple. Since calibrations published in reference 16 and repeated here in figure 9 showed the thermoelectric properties of Niculoy 22/constantan to be very similar to copper/constantan (within ±2 percent at the temperature range considered), the properties of the latter were used to reduce the data.

Data Reduction

The tile heating response at the "T" gap indicated that the maximum heating rate occurred before the model reached the tunnel centerline but after the model reached the edge of the core of uniform flow 24 in. from the tunnel centerline. (See fig. 10.) The cold-wall heating rates presented herein were taken at the time when the peak heating rate occurred in the "T" gap region.

Model and tunnel data were recorded by a high-speed digital recorder at 20 frames per second through 10-Hz filters. Cold-wall heating rates were calculated from these outputs by using the one-dimensional transient heat-balance equation $\dot{q} = \rho c_p \tau (\mathrm{d}T/\mathrm{d}t)$, where $\mathrm{d}T/\mathrm{d}t$ was determined from a 5-point central difference approximation to smooth out noise in the data channels.

The one-dimensional heat-balance equation equates the convective heat transfer to the surface to the energy stored, with the effect of conduction and radiation assumed to be negligible. These assumptions are considered reasonable since the temperature-time slopes were taken early in the tests when the surface temperatures and spatial gradients were relatively low. Also, the relative magnitude of the effect of neglecting the conduction and radiation terms can be calculated by including these terms in the heat-balance equation and then deleting the terms individually. This analysis indicated a maximum error in the heat flux of less than 17 percent in the high-temperature-gradient "T" gap region and of approximately zero in all other areas.

To calculate the total heat load to the simulated Shuttle tile from the experimental data, it was necessary to interpolate first the data to a regular grid (ref. 17) to permit the use of standard numerical integration techniques. The center tile was instrumented with 256 thermocouples on the top and the four vertical sides to within 0.5 in. of the bottom of the intertile gap. Each surface was gridded in increments of 0.1 in., and the limited number of thermocouples was located to the best advantage on this grid. Most of the thermocouples were concentrated along the tile edges and in the other areas where high thermal gradients were expected. The rest were scattered sparsely over the remaining areas of the tile to complete coverage of the tile surface. The resulting distribution of test data was very irregular, and techniques for random data were employed to interpolate the data to a regular grid separately for each face. An algorithm developed by Akima (ref. 18) was used to perform a triangulation of the data and to generate a temperature surface through the two-dimensional array of data points. A fifth-degree bivariate polynomial was determined by estimated values of the partial derivatives at the data points at the vertices of each triangle and was used to interpolate the data to the same grid used to locate the thermocouples.

This algorithm proved to be sensitive to sparse data regions. For several test cases, undulations were present in the interpolated data in regions where the approximating surface to the data was expected to be uniform. To remedy the situation, the data were interpolated to a coarse grid derived from the fine grid but designed to avoid the areas where the Akima algorithm did not perform well. The grid lines of the original grid with 0.1 in. resolution were examined individually. Any line with three or more data points whose distribution along the line spanned one-half to two-thirds of the total distance across the tile was included in the new grid. As a result, the grid lines were unequally spaced in both x and y, with the majority of grid lines being concentrated in the data-rich areas and with only a few in the data-sparse areas. To enrich the data-sparse areas, this relatively coarse grid was interpolated back to the original fine grid by using bicubic splines.

The interpolated data were checked at each step to make sure that the new values were consistent with the measured values. Agreement between the interpolated and measured values was very good in most cases. Most discrepancies were the result of the lack of data on the vertical sides due to either thermocouple failure or to an insufficient number of data points to resolve the high gradients in the regions that experienced high heating rates. For instance, in the highly heated areas the heating rates tended to be overestimated since the slope of the surface generated for interpolation did not decrease rapidly enough. However, this problem was limited

to very small areas of the tile and did not contribute a significant error to the total heating rate of the tile. The thermocouples that failed during the test series were located near the lower edge of the grid on the vertical sides. Since fewer thermocouples were originally installed in these areas, their failure produced a serious lack of data for larger areas of the sides. Rather than extrapolate data to these areas, reasonable estimates for these thermocouples were substituted instead.

The interpolated data on the fine grid were then integrated by using a nine-point two-dimensional Simpson's rule. This algorithm is exact for cubic polynomials so that the accuracy of the method in this case depends on the accuracy to which the cubic splines represent the surface defined by the heating-rate data. Except for the edges that were averaged, each surface of the tile was integrated separately. The total heating rate was calculated by adding the contribution from each face.

The experimental data are presented as nondimensional ratios of the experimental heating rates and a corresponding theoretical flat-plate heating rate. The theoretical flat-plate heating rates were based on Eckert's reference temperature and were used instead of calibration data to account for variations in the tunnel flow conditions. Also, the theoretical values agreed well with flat-plate calibration data. The flat-plate total heat loads were obtained by multiplying the theoretical flat-plate heating rate by the top surface area of the instrumented tile. These data are presented in table III.

Results and Discussion

Aerodynamic Heating in Laminar Flow

Tests were conducted under laminar-flow conditions to identify overall and local flow characteristics and to determine the effects of gap geometry on the magnitude and distribution of convective heating in the "T" gap region and on the upstream corner. All the laminar data were obtained at a nominal $T_{t,c}$ of 3100°R, a nominal q_∞ of 2.2 psia, and at $\alpha = 0°$. In this section the stem of the "T" will be defined as the longitudinal gap and the cap of the "T" will be defined as the transverse gap.

Localized heating. Typical aerodynamic heating-rate distributions on the upstream corner and the "T" gap are shown for laminar flow in figure 11 for $\Lambda = 0°$, 45°, and 60° with $W = 0.070$ in. and $\Lambda = 45°$ with $W = 0.160$ in. The heating rates along the intersection of sides 1 and 4 (see fig. 7) to the center of the top surface and at the "T" gap region to the tile center are nondimensionalized by the flat-plate heating rate. The low heating rates in the gaps indicate that hot gas from the laminar boundary layer does not readily penetrate the gaps. At a value of B/H of approximately 0.9 and $\Lambda = 45°$ (fig. 11(b)), the heating rates increase rapidly and peak at approximately 2.0 times the flat-plate value on the top surface just behind the tile edge radius. Apparently, for laminar flow most of the flow bridges the gap and attaches on the top surface. From this attachment point the heating decreases to the flat-plate value. For $\Lambda = 60°$ (fig. 11(c)), the heating has a peak on the edge radius; however, it appears as though a disturbance caused the heating to begin increasing again on the top surface. This disturbance may actually be a transitioning of the laminar flow. It was noted in reference 11 that the gaps tend to trip the laminar flow to transitional flow. Considering these facts, it is felt that the increased heating on the top surface of the tile was caused by transitional flow. Therefore, in laminar flow only a small amount of relatively low energy flow enters the gap and most of the heating effect is confined to the portion of the gap near the top. This suggests that both gas temperature and velocity decay rapidly with distance from the surface. Previous results at $\Lambda = 0°$ (ref. 11) indicated similar results.

In this report, thermocouples 1 and 9 were chosen to represent the heating characteristics in the corner and "T" gap regions, respectively. Thermocouples 1 and 9 are located on the midarc of the corresponding edge radii. Other thermocouples in these regions show similar trends.

The effects of flow angularity on the heating rates at the corner and "T" gap are shown in figure 12 for $W = 0.070$ in. The curves represent least-squares first-order polynomial fits to the data. Because of the low-energy content of the flow penetrating into the tile gaps, local heating rates are insensitive to flow angle changes from 0° to 60°. In general, the heating at the "T" gap is greater than at the corner. Also, the heating increases slightly at the corner but remains relatively constant at the "T" gap with increasing Λ.

The effect of gap width on heating rates at the corner and "T" gap are shown in figure 13 for $\Lambda = 45°$. The data indicate that the local peak heating increases moderately because of increases in the gap width. The heating at the corner and "T" gap increases linearly with gap width and, for these tests, increases approximately 36 percent as the gap width is increased from 0.040 to 0.160 in. Previous studies (ref. 11) at a flow angle of 0° and with the forward-facing tile wall sloped backward 15° off vertical indicate that an increase in heating of 243 percent may

occur in the "T" gap region as the gap width is increased from 0.040 to 0.160 in. for laminar flow.

Overall tile heating. Heating distributions on the front face and sides of the tile are shown in figures 14 and 15, respectively. Typical heating distributions across the front face (side 1) of the instrumented tile at various depths near the top of the gap are shown in figure 14. Data are shown for $\Lambda = 0°$, 45°, and 60° with $W = 0.070$ in. and for $\Lambda = 45°$ with $W = 0.160$ in. In general, the heating is highest along the edge radius. When $\Lambda = 0°$ the heating across side 1 is fairly symmetrical. However, when the tile is rotated so that $\Lambda = 45°$ (fig. 14(b)), the heating increases along the gap length. From comparing figures 14(a) and 14(b) (with heating at locations $y = 0.2$, 0.3, and 0.6 in.), it is seen that the local heating is decreased because there is less flow in the longitudinal gap because of the rotation, and hence not as much flow is diverted down into the gap. When the tile is rotated such that $\Lambda = 60°$ (fig. 14(c)), the transverse gap is more nearly aligned with the flow. This produces a longer uninterrupted effective gap length, which allows more flow to penetrate into the gap. Therefore, the heating increases along the gap length and depth.

A comparison between figures 14(b) and 14(d) (with $\Lambda = 45°$) also shows that an increase in W increases the heating in the gap. This was also shown in figure 13. In all cases there are deviations in the heating rates around the centerline of side 1, which is the intersection of the longitudinal and transverse gaps. The mixing of flow in these two gaps sets up a three-dimensional flow pattern that changes with any change in the geometric parameters. The blocking tile forces flow over the top of the tile, deeper into the gaps, and in both directions in the transverse gap. This fluctuation in heating appears to be a local deviation from the characteristic two-dimensional flow for laminar flow reported in reference 11. The deviations were probably caused by local disturbances created by the "T" gap causing the local flow to be more three-dimensional. Limited data from reference 11 show that this type of deviation in heating rates can occur for larger gap widths and forward-sloped walls (the same flow orientation as side 1). However, the deviations should be more severe for vertical walls.

Peripheral distributions at three depths into the gap ($y = 0.03, 1.0$, and 2.0 in.) are compared in figure 15, which shows data for $\Lambda = 0°$, 45°, and 60° with $W = 0.070$ in. and for $\Lambda = 45°$ with $W = 0.160$ in. The heating at $y = 0.03$ in. is considerably greater than at $y = 1.0$ and 2.0 in. This is also seen in figure 11 where the laminar boundary-layer data indicated that only a small amount of relatively low energy flow enters the gaps. Comparisons of the absolute heating levels are difficult because the heating levels are so low for $y = 1.0$ and 2.0 in. Heating distributions at $y = 0.03$ in. show that the heating on side 1 is greater than on sides 2, 3, and 4, except when $\Lambda = 60°$ where side 4 is greater. With $\Lambda = 60°$, side 4 is more perpendicular to the flow; however, there is no gap perpendicular to side 4 ("T" gap) to channel additional flow. The most likely explanation for this increased heating is that the tile adjacent to side 4 was slightly depressed, thus leaving a slight forward-facing step with flow impinging on that side at an angle of 30°. Small misalignments can cause considerable heating, as will be discussed in the subsequent section "Effect of forward-facing step on heating."

Overall heating distributions can best be seen in figure 16 in which interpolated heating rates are presented in color graphic displays. Data are presented for $\Lambda = 0°$, 45°, and 60° with $W = 0.070$ in. and for $\Lambda = 45°$ with $W = 0.160$ in. The exploded views of the tile show the details on the hidden sidewalls. The color scale below the figure relates the colors to the absolute and nondimensionalized heating rate. The heating to the lower 1/2 in. of the tile is not displayed because all the thermocouples below that point were damaged during the fabrication process. The representation of the tile heating in figure 16 shows that the heating to the tile is fairly uniform over the top surface for all cases. Note the scale changes because of varying heating levels. However, for $\Lambda = 60°$ the top surface heating is almost twice that of $\Lambda = 0°$ (figs. 16(a) and 16(d) and table III). This phenomenon will be discussed later. Once again, observe that the heat input to the sidewalls is low because of the low-energy content of the flow in the gaps. With flow angles of 45° (figs. 16(b) and 16(c)), no significant change in the heating distribution is seen from $\Lambda = 0°$, thus indicating the insensitivity of the heating in laminar flow to changes in Λ. Note that there is no increase in heating to side 1 due to the upstream "T" gap with flow angles of 0°, 45°, and 60°. These data substantiate previous findings in which the laminar external flow that penetrates into the gaps creates a basically two-dimensional heating distribution.

The heating rates were numerically integrated over the tile surface to get the heat load to each surface and the total heat load to the tile. Surface and total heat loads are given in table III. The effect of flow angularity on the total heat load to the tile is shown graphically in figure 17 for $W = 0.070$ in. The total heat load is nondimensionalized by the total heat load for a flat plate with the planform area equal to the tile top surface. The total heat

load to the tile remains relatively constant at an average of twice the flat-plate value. It is important to note that the surface areas of the four sidewalls represent 62 percent of the total surface area. This large surface area results in the increased total heat load to the tile over the flat-plate value even with the very low heating rates. For instance, at $\Lambda = 45°$ the total heat load to the tile is 1.83 times the equivalent flat-plate heat load, with approximately 1.43 times Q_{FP} of the heat load from the top surface and 0.40 times Q_{FP} from the sidewalls. At $\Lambda = 60°$ the total heating on the top surface increased dramatically (table III) to produce a total heat load 3.1 times the flat-plate load. This increase is due to an increase in surface heating, not to an increase of heating in the gaps. Since the heating is greater than laminar but less than turbulent levels, the flow is believed to be transitional.

The effect of gap width W on the total heat load is shown in figure 18 for $\Lambda = 45°$. The total heating appears to decrease as the gap width is increased from 0.040 to 0.160 in. This trend reflects events happening to the top surface as the sidewall heating is essentially constant. No great significance is placed on this trend because of the limited data, and the deviation over the gap-width range is within the accuracy of the measurement technique.

Aerodynamic Heating in Turbulent Flow

Tests were conducted under turbulent-flow conditions to identify overall and local flow characteristics and to determine the magnitude and distribution of the convective heating in the "T" gap region and on the upstream corner as affected by gap geometry. Turbulent-heating data were collected with a nominal $T_{t,c}$ of 3200°R, q_∞ between 1.8 and 9.0 psia, and $\alpha = 0°$ or 7.5°. Data are presented for a nominal q_∞ of 2.2 psia with a blunt leading edge on the panel holder (designated low-energy turbulent flow that results from the nonisentropic normal shock ahead of the blunt leading edge) and for a $q_\infty = 3.5$ psia with a sharp leading edge on the panel holder (designated high-energy turbulent flow that results from the nearly isentropic oblique shock attached to the sharp leading edge). One test with a nominal step height of approximately 0.035 in. is discussed at the end of this section.

Localized heating. Typical aerodynamic heating distributions on the upstream corner and the "T" gap are shown for turbulent flow in figures 19 and 20 for $\Lambda = 0°$, 45°, and 60° with $W = 0.070$ in. and for $\Lambda = 45°$ with $W = 0.160$ in. The heating rates along the intersection of sides 1 and 4 to the center of the top surface and at the "T" gap region to the tile center are nondimensionalized by the flat-plate heating rate. Heating distributions for low-energy turbulent flow (fig. 19) are similar to laminar flow in that the flow does not readily penetrate the gaps. Above $B/H = 0.9$ the heating rates increased rapidly and peaked on the top edge radius or just behind the radius. The peak heating was approximately equivalent to the theoretical flat-plate heating rate at the center of the tile. Laminar flow peaked at higher ratios; however, the absolute values were lower. Heating distributions on the the upstream corner and the "T" gap are characterized for high-energy turbulent flow in figure 20. Data are presented for $W = 0.070$ in. and $\Lambda = 0°$, 45°, and 60°. At $B/H = 0.9$, heating increased very rapidly and peaked on the top edge radius and the top surface. The magnitude of the peak heating is considerably different from the heating in laminar flow and low-energy turbulent flow. In high-energy turbulent flow the impinging flow produces a well-defined region of high localized heating. This will be discussed subsequently in more detail. For $\Lambda = 0°$, flow in the longitudinal gap impinged directly on the instrumented front face and, therefore, produced the highest localized impingement heating. The peak heating in the "T" gap region was 9.5 times the flat-plate heating rate. However, the flow did not impinge directly on the corner, and hence the heating was equivalent to the flat-plate heating. As the flow angle was increased, the heating in the "T" gap was drastically reduced and the corner heating was increased. This will be discussed in greater detail later. However, in all cases the heating quickly returned to a uniform heating value equivalent to the flat-plate heating value.

As in the results from reference 11, the maximum heating occurs somewhere on the edge radius. Herein, thermocouples 1 and 9 were chosen again to represent the maximum heating in the corner and "T" gap regions, respectively. Thermocouples 1 and 9 are located on the midarc of the corresponding edge radii. Other thermocouples in these regions show similar trends.

The effects of flow angularity on the heating rates at the corner and "T" gap are shown in figure 21 for $W = 0.070$ in. As for laminar flow, low-energy turbulent flow produces heating that is relatively insensitive to increases in flow angle. However, for high-energy turbulent flow, increasing the flow angle from 0° to 60° significantly reduces the high localized heating in the "T" gap region by decreasing the amount of flow in the longitudinal gap, thus decreasing the flow impinging in the "T" gap region. At a flow angle of 0°, the maximum heating in the "T"

gap region was 9.5 times the flat-plate heating rate. The heating decreases rapidly with increasing flow angle to a minimum measured value of 1.9 times the flat-plate heating at a flow angle of approximately 45°. The heating in the "T" gap at $\Lambda = 60°$ has increased to approximately 2.1 times the $\dot{q}_{FP}$. This increase in heating is attributed to increased flow in the transverse gap as the external flow becomes more closely aligned with the transverse gap. The results from reference 7 show significant increased heating for aligned tile arrays ($\Lambda = 90°$).

The corner heating is lowest for a flow angle of 15° and reaches a peak value 3.2 times the flat-plate heating rate at $\Lambda = 60°$. Similar to the "T" gap heating, the corner heating would probably continue to increase as Λ exceeded 60° because the continuous transverse gaps would allow significant entrained flow and attendant increased heating at the corner and on the sidewalls. The data suggest orienting the tile so that the local flow angle is between 30° and 50° to minimize the high localized heating. The baseline Shuttle tile orientation of 45° provides some margin to accommodate local flow-angle changes during entry.

Previous studies for turbulent flow with $\Lambda = 0°$ indicate that the peak heating in the "T" gap increases with approximately the 0.4 power of the gap width (ref. 11). Present laminar-flow data at $\Lambda = 45°$ (fig. 13) indicate a 36-percent increase in heating when W is increased from 0.040 to 0.160 in. However, present low-energy turbulent-flow data at $\Lambda = 45°$ (fig. 22) indicate that heating in the corner and "T" gap region (TC-1 and TC-9, respectively) decreases with increasing gap width. This trend is also supported by data on the upper left side of side 1. (See cross-hatched area of figure insert.) However, all other data (for example, TC-127) on the front face show an upward trend with increasing gap width. This decreased heating at $\Lambda = 45°$ is therefore a local heating effect. The upstream tile corner may be raised slightly or may be creating a flow disturbance that influences this area. These disturbances could also contribute to the deviations in the data.

Overall tile heating. Heating distributions at various gap depths are shown in figures 23 to 26. These figures also support the conclusions reached in the previous section. Typical heating distributions across the front face (side 1) of the instrumented tile at various depths near the top of the gap are shown in figure 23 for low-energy turbulent flow. Data are shown for $\Lambda = 0°$, 45°, and 60° with $W = 0.070$ in. and for $\Lambda = 45°$ with $W = 0.160$ in. These data show the same trends as those seen in laminar flow. The nondimensionalized heating levels are less than those in laminar flow; however, the absolute levels are higher. The heating is highest along the edge radius. In this case heating along the midarc does not have the symmetrical behavior expected for $\Lambda = 0°$. When the tile is rotated so that $\Lambda = 45°$ or 60°, the heating increases with gap length (increasing S). Also, the heating down in the gap is decreased as Λ increases.

Heating distributions near the top of the gap on side 1 for high-energy turbulent flow are shown for $W = 0.070$ in. and $\Lambda = 0°$, 45°, and 60° in figure 24. The heating distributions vary over a much wider range than in the low-energy laminar- or turbulent-flow cases. A slight tile misalignment probably caused the unsymmetrical behavior of the edge-radius data when $\Lambda = 0°$; otherwise the front-face heating is symmetrical about the centerline as reported in reference 11. In contrast to low-energy laminar and turbulent flow, these data show a relatively uniform heating along the gap length (increasing S). Figure 24(c) shows a substantial increase in heating at the corner between $S = 0$ and 0.5 in. This increase was most likely caused by the corner of the instrumented tile slightly protruding out into the transverse gap.

The peripheral heating distributions for low-energy turbulent flow at three depths into the gap ($y = 0.03$, 1.0, and 2.0 in.) are shown in figure 25. Again, the nondimensionalized heating levels for low-energy turbulent flow are comparable with laminar flow (fig. 15). However, in this case heating on side 1 is always greater than heating on the other three sides. Also, at flow angles other than 0° for side 4 and with $y = 0.03$ in., an increase in heating is seen as S increases to the upstream tile corner.

High-energy turbulent-flow comparisons are shown in figure 26. Normalized data at and below $y = 1.0$ in. is very low, and this figure shows only the relative difference in magnitude between the heating at the three gap depths. For $\Lambda = 0°$ (fig. 26(a)), the heating on sides 2 and 4 is equivalent. The condition having sides 2 and 4 with $\Lambda = 0°$ is the only arrangement in which the model has a symmetrical geometry. The high heating at the upstream corner is again seen when $\Lambda = 45°$ and 60°.

Overall heating distributions can best be seen in figures 27 and 28 in which interpolated heating rates are presented in color graphic displays. Data are presented for $\Lambda = 0°$, 45°, and 60° with $W = 0.070$ in. and for $\Lambda = 45°$ with $W = 0.160$ in. for low-energy turbulent flow and for $\Lambda = 0°$, 45°, and 60° with $W = 0.070$ in. for high-energy turbulent flow. The exploded view of the tile shows the details on the hidden sidewalls. The color scale below the figures relates the colors to the absolute and nondimensionalized heating rate. The heating to the

lower 1/2 in. of the tile is not displayed because all the thermocouples below that point were damaged during the tile fabrication process.

For low-energy turbulent flow, figure 27 shows no significant change in the heating patterns. An asymmetrical heating pattern is also shown in figure 27. This was caused by a tile misalignment that can best be seen in the high-energy turbulent data. Significant changes in the heating patterns as a function of Λ can be seen in figure 28 for high-energy turbulent flow. Because the localized heating regions occur over a small area, all heating rates above 20 Btu/ft^2-sec are assigned to the color *white*. Note the scale changes (fig. 28) because of significant changes in heating levels. For $\Lambda = 0°$ (fig. 28(a)), the heating on the top surface is generally uniform except along the edge where the top surface and side 1 intersect. This further illustrates the high flux gradients shown in figures 20, 24, and 26. The increased heating contours for the sidewalls indicate that the turbulent flow penetrates farther into the gaps and has a higher energy content than low-energy laminar or turbulent flow. The highest localized heating (9.5 times $\dot{q}_{FP}$) occurred at the center of the front face at the end of the "T" gap for $\Lambda = 0°$. The high heating to the right of the "T" gap was caused by a slight tile misalignment. The tile upstream of the instrumented tile was depressed (detected after the test), resulting in a forward-facing step of 0.010 in. The significant heating difference on either side of the "T" gap illustrates the sensitivity of the heating to slight misalignments. The left and right sidewalls show evidence of deeper flow penetration into the gaps as the flow moves along a side (longitudinal) gap. At flow angles of 45° and 60° (figs. 28(b) and 28(c), respectively), the high localized heating to the "T" gap is significantly less than the heating for $\Lambda = 0°$, and the overall heating levels also decreased. It appears in figure 28(c) that the heating in the corner has increased over the heating in the corner for $\Lambda = 0°$ (fig. 28(a)). Because of the scales, this is difficult to distinguish; however, subsequent figures will show this to be the case.

As for laminar-flow tests, the local heating rates were numerically integrated over each surface to obtain total heat loads. The results are presented in table III. The effect of flow angularity on the total heat load to the tile is shown in figure 29 for $W = 0.070$ in. Although the heating rates for low-energy turbulent flow are approximately twice those for laminar flow, the trends show that the total heating is insensitive to changes in flow angle. At $\Lambda = 0°$, the total heat load to the tile for high-energy turbulent flow (fig. 29(b)) is 2.2 times the heat load to the equivalent flat-plate area. The top-surface heat load is 1.8 times the heat load to a smooth surface, and the total heat load to the four sidewalls is 0.4 times Q_{FP}. In contrast, at $\Lambda = 45°$ the total heat load to the tile is 1.37 times the flat-plate heat load, the heat load to the top surface is 1.29 times the flat-plate heating, and the sidewalls are 0.13 times Q_{FP}. The total heat load, as well as the heat load to the top and sidewalls, generally decreases with increasing flow angle. However, as indicated in figure 21 for the "T" gap region, the heating reaches a minimum between $\Lambda = 30°$ and 40° as the flow angle is increased. As the flow angle is increased further, more flow penetrates into the transverse gap, thus increasing the sidewall heating and therefore the total heat load. As stated earlier, this increase is supported by reference 7 in which aligned tile arrays ($\Lambda = 90°$) experienced a total heat load 40 percent higher than that of a staggered tile arrangement ($\Lambda = 0°$). In general, rotating the tile about the tile center surface normal decreases the heating to the tile, reduces the localized heating in the "T" gap region, and hence reduces the flow in the gaps, thus reducing the total heat load.

The effect of gap width (0.040 to 0.160 in.) on the total heat load is shown in figure 30 for $\Lambda = 45°$. As indicated by the least-squares first-order polynomial fit to the data, only a slight decrease in total heat load occurs with increasing W for low-energy turbulent flow (fig. 30(a)), as was the case with laminar flow. This result was not expected, but a localized heating region (upper left side of side 1) experienced the same effects at $\Lambda = 45°$. (See fig. 22.) Only two test points exist for high-energy turbulent flow (fig. 30(b)); however, the slope of the data indicates similar results.

Effect of forward-facing step on heating. For test 19 the top surface of the instrumented tile was inadvertently installed higher than the surrounding tiles, thus producing a nominal forward-facing step of 0.035 in. (one-half the gap width). Also, the two tiles upstream of the instrumented tile were not at exactly the same level; therefore, the heating on the instrumented tile was not symmetric. The forward-facing step in high-energy turbulent flow with $\Lambda = 0°$ resulted in high heating along the entire top edge of side 1 instead of only the localized heating observed in the no-step case. The heating distribution across side 1 at various depths in the transverse gap is shown in figure 31(a). The high localized heating still existed in the "T" gap region and decreased rapidly from this point to a relatively uniform level out to the vertical edges of the tile. The ratio of the heating due to the forward-facing step to the heating with no forward-facing step shows the effect of a forward-

facing step on the front-face heating (fig. 31(b)). At $S = 2.95$ in. (centerline of side 1), the heating ratio is approximately 1, thus indicating little effect on local "T" gap heating due to the step. However, the step permitted direct impingement of the external flow on the raised portion of the tile and increased mass flow in the transverse gap, hence causing higher heating away from the "T" gap region and at greater depths. The maximum local increase in heating due to the step was 3.9 times the heating for a no-step case and occurred near the tile corner.

Concluding Remarks

The heat transfer to simulated Shuttle thermal protection system tiles has been investigated experimentally by using a highly instrumented metallic thin-wall tile arranged with other metal tiles in a staggered tile array. This tile arrangement results in longitudinal gaps terminating at intersections with transverse gaps (referred to as "T" gaps). This study extends previous efforts by including the effect of the flow angularity on localized heating in the "T" gap and upstream tile corner. Flow angles investigated include 0°, 15°, 30°, 45°, and 60°. Cold-wall heating-rate data (calculated by using the thin-wall technique) for laminar and turbulent flow were obtained in the Langley 8-Foot High-Temperature Tunnel at a nominal Mach number of 7, a nominal total temperature of 3300°R, a free-stream unit Reynolds number from 3.4×10^5 to 2.2×10^6 per foot, and a free-stream dynamic pressure from 2.1 to 9.0 psia.

For a laminar boundary layer, the overall heating data indicate that the flow penetrating the gaps has a low-energy content. In general, total heating is insensitive to changes in gap width and flow angle. Increasing the gap width when the flow angle is 45° does not cause a variation on local heating that is as large as at a flow angle of 0°. The total heat load is approximately 60 percent greater than the equivalent flat-plate heat load; however, this increase is caused by the increased surface area from the sidewalls.

Heating distributions obtained in low-energy turbulent boundary layers are similar to those obtained in laminar flow in that the flow penetrating the gaps has a low-energy content and does not produce high localized heating in the "T" gap region. Also, the local and total heating are relatively insensitive to changes in flow angle. The total heat load also decreased slightly with increasing gap width, as was the case with laminar flow.

For high-energy turbulent boundary layers, higher energy flow penetrated deeper into the gaps, thus creating higher localized heating at the corner and "T" gap regions than for low-energy laminar or turbulent flow. Increasing the flow angle with respect to the longitudinal gap significantly reduced the high localized heating in the "T" gap region and moderately increased the localized heating at the corner region. These data suggest orienting the tiles such that the local flow angle is between 30° and 50° to minimize the localized heating. Misalignment of the instrumented tile, producing a maximum forward-facing step of one-half the gap width, resulted in high localized heating along the top edge of the front face of the tile. This illustrates the sensitivity of the heating to surface misalignment in the form of forward-facing steps. For a gap width of 0.070 in. and no step, the total heat load to the tile was as much as 36 percent greater than the heat load to the equivalent flat-plate area. In general, rotating the tile about the tile center surface normal decreases the heating to the tile, reduces the localized heating in the "T" gap region, and hence reduces the flow in the gaps, thus reducing the total heat load.

NASA Langley Research Center
Hampton, VA 23665
March 12, 1985

References

1. Anderson, Roger A.; Brooks, William A., Jr.; Leonard, Robert W.; and Maltz, Joseph: Structures—A Technology Overview. *Astronaut. & Aeronaut.*, vol. 9, no. 2, Feb. 1971, pp. 38–47.
2. Emde, Wendall D.: Thermal Protection System for the Shuttle Orbiter. *Bicentennial of Materials Progress*, Volume 21 of National SAMPE Symposium and Exhibition, Soc. Advance. Mater. & Process. Eng., 1976, pp. 964–978.
3. Goldstein, Howard E.: Fibrous Ceramic Insulation. *Advanced Materials Technology*, Charles P. Blankenship and Louis A. Teichman, compilers, NASA CP-2251, 1982, pp. 261–274.
4. Brewer, R. A.; Saydah, A. R.; Nestler, D. E.; and Florence, D. E.: Thermal Performance Evaluation of RSI Panel Gaps for Space Shuttle Orbiter. *J. Spacecr. & Rockets*, vol. 10, no. 1, Jan. 1973, pp. 23–28.
5. Dunavant, James C.; and Throckmorton, David A.: Aerodynamic Heat Transfer to RSI Tile Surfaces and Gap Intersections. *J. Spacecr. & Rockets*, vol. 11, no. 6, June 1974, pp. 437–440.
6. Christensen, H. E.; and Kipp, H. W.: *Data Correlation and Analysis of Arc Tunnel and Wind Tunnel Tests of RSI Joints and Gaps. Volume I—Technical Report.* NASA CR-134345, 1974.
7. Weinstein, Irving; Avery, Don E.; and Chapman, Andrew J.: *Aerodynamic Heating to the Gaps and Surfaces of Simulated Reusable-Surface-Insulation Tile Arrays in Turbulent Flow at Mach 6.6.* NASA TM X-3225, 1975.

8. Throckmorton, David A.: *Pressure Gradient Effects on Heat Transfer to Reusable Surface Insulation Tile-Array Gaps.* NASA TN D-7939, 1975.
9. Throckmorton, David A.: *Effect of a Surface-to-Gap Temperature Discontinuity on the Heat Transfer to Reusable Surface Insulation Tile Gaps.* NASA TN D-8233, 1976.
10. Hunt, L. Roane; Shideler, John L.; and Weinstein, Irving: *Performance of LI-1542 Reusable Surface Insulation System in a Hypersonic Stream.* NASA TN D-8150, 1976.
11. Avery, Don E.: *Aerodynamic Heating in Gaps of Thermal Protection System Tile Arrays in Laminar and Turbulent Boundary Layers.* NASA TP-1187, 1978.
12. Avery, Don E.; Ballard, Gary K.; and Wilson, Maywood L.: *Electroless-Plating Technique for Fabricating Thin-Wall Convective Heat-Transfer Models.* NASA TP-2349, 1984.
13. Deveikis, William D.; Bruce, Walter E., Jr.; and Karns, John R.: *Techniques for Aerothermal Tests of Large, Flightweight Thermal Protection Panels in a Mach 7 Wind Tunnel.* NASA TM X-71983, 1974.
14. Deveikis, William D.; and Hunt, L. Roane: *Loading and Heating of a Large Flat Plate at Mach 7 in the Langley 8-Foot High-Temperature Structures Tunnel.* NASA TN D-7275, 1973.
15. Schaefer, William T., Jr.: *Characteristics of Major Active Wind Tunnels at the Langley Research Center.* NASA TM X-1130, 1965.
16. Stalmach, C. J., Jr.: *Developments in Convective Heat Transfer Models Featuring Seamless and Selected-Detail Surfaces, Employing Electroless Plating.* Tech. Rep. 2-57110/5R-3227 (Contract NAS9-13692), Vought Syst. Div., LTV Aerospace Corp., June 30, 1975. (Available as NASA CR-144364.)
17. Greville, T. N. E.: Spline Functions, Interpolation, and Numerical Quadrature. *Mathematical Methods for Digital Computers*, Volume II, Anthony Ralston and Herbert S. Wilf, eds., John Wiley & Sons, Inc., c.1967, pp. 156–168.
18. Akima, Hiroshi: A Method of Bivariate Interpolation and Smooth Surface Fitting for Irregularly Distributed Data Points. *ACM Trans. Math. Software*, vol. 4, no. 2, June 1978, pp. 148-159.

TABLE I. THERMOCOUPLE LOCATIONS

Thermocouple	x, in. (a)	y, in. (a)	z, in. (a)	Thermocouple	x, in. (a)	y, in. (a)	z, in. (a)	Thermocouple	x, in. (a)	y, in. (a)	z, in. (a)
1	0.03	0.03	0.03	26	2.95	0.03	0.10	51	0.03	0.03	0.60
2	.10	↓	↓	27	3.00	↓	↓	52	.10	↓	↓
3	.20			28	3.10			53	.20		
4	.30			29	3.60			54	.40		
5	.60			30	4.20			55	1.80		
6	1.20			31	5.40			56	3.00		
7	2.80			32	.03		.20	57	4.20		
8	2.90			33	.10		↓	58	5.40		
9	2.95			34	.30			59	5.80		
10	3.00			35	1.20			60	.03		1.20
11	3.10			36	1.80			61	.20		↓
12	3.60			37	2.40			62	1.20		
13	4.80			38	2.90			63	2.40		
14	5.40			39	3.00			64	3.60		
15	5.80		↓	40	5.80		↓	65	4.80		
16	0		.10	41	.03		.30	66	5.80		
17	.10		↓	42	.10		↓	67	.10		1.80
18	.20			43	.20			68	.20		↓
19	.30			44	.30			69	.40		
20	.40			45	.60			70	1.80		
21	.60			46	.10		.40	71	3.00		
22	1.80			47	.40		↓	72	4.20		
23	2.40			48	1.20			73	5.40		
24	2.80			49	2.40			74	5.80		
25	2.90	↓	↓	50	5.80	↓	↓	75	.10	↓	2.40

[a]See figure 7.

TABLE I. Continued

Thermocouple	x, in. (a)	y, in. (a)	z, in. (a)	Thermocouple	x, in. (a)	y, in. (a)	z, in. (a)	Thermocouple	x, in. (a)	y, in. (a)	z, in. (a)
76	0.20	0.03	2.40	101	1.80	0.03	5.40	126	3.40	0.10	0.03
77	2.40	↓	↓	102	3.00	↓	↓	127	4.20	.10	↓
78	3.60	↓	↓	103	4.20	↓	↓	128	5.40	.10	↓
79	4.80	↓	↓	104	5.40	↓	↓	129	.03	.20	↓
80	.10	↓	3.00	105	.10	↓	6.00	130	.10	↓	↓
81	.20	↓	↓	106	.30	↓	↓	131	.20	↓	↓
82	.60	↓	↓	107	.60	↓	↓	132	2.80	↓	↓
83	1.80	↓	↓	108	3.00	↓	↓	133	2.95	↓	↓
84	2.40	↓	↓	109	5.40	↓	↓	134	3.10	↓	↓
85	3.00	↓	↓	110	.10	↓	6.34	135	.03	.30	↓
86	4.20	↓	↓	111	.30	↓	↓	136	.20	↓	↓
87	5.40	↓	↓	112	.60	↓	↓	137	.40	↓	↓
88	.03	↓	3.60	113	1.40	↓	↓	138	2.50	↓	↓
89	.10	↓	↓	114	.03	.10	.03	139	2.70	↓	↓
90	3.60	↓	↓	115	.10	↓	↓	140	2.90	↓	↓
91	4.80	↓	↓	116	.40	↓	↓	141	2.95	↓	↓
92	.03	↓	4.20	117	.60	↓	↓	142	3.00	↓	↓
93	.10	↓	↓	118	1.20	↓	↓	143	3.20	↓	↓
94	3.00	↓	↓	119	1.80	↓	↓	144	3.40	↓	↓
95	4.20	↓	↓	120	2.40	↓	↓	145	.03	.40	↓
96	5.40	↓	↓	121	2.70	↓	↓	146	.10	.40	↓
97	.03	↓	4.80	122	2.90	↓	↓	147	.20	.40	↓
98	4.80	↓	4.80	123	2.95	↓	↓	148	.03	.60	↓
99	.03	↓	5.40	124	3.00	↓	↓	149	.20	.60	↓
100	.60	↓	5.40	125	3.20	↓	↓	150	.40	.60	↓

[a]See figure 7.

TABLE I. Continued

Thermocouple	x, in. (a)	y, in. (a)	z, in. (a)	Thermocouple	x, in. (a)	y, in. (a)	z, in. (a)	Thermocouple	x, in. (a)	y, in. (a)	z, in. (a)
151	2.70	0.60	0.03	176	0.03	0.10	1.80	201	0.03	0.03	6.44
152	2.95	↓	↓	177	↓	↓	2.40	202	.30	↓	↓
153	3.10	↓	↓	178	↓	↓	3.00	203	.60	↓	↓
154	3.20	↓	↓	179	↓	↓	3.60	204	1.40	↓	↓
155	.03	1.00	↓	180	↓	↓	6.00	205	3.00	↓	↓
156	.20	↓	↓	181	.20	.10	↓	206	4.20	↓	↓
157	1.20	↓	↓	182	.20	.20	↓	207	5.60	↓	↓
158	2.40	↓	↓	183	.30	.20	↓	208	5.90	↓	↓
159	2.95	↓	↓	184	.30	.40	↓	209	.03	.20	↓
160	3.60	↓	↓	185	.40	.10	↓	210	.30	↓	↓
161	4.80	↓	↓	186	.40	.20	↓	211	.60	↓	↓
162	.03	1.50	↓	187	.60	.20	↓	212	1.40	↓	↓
163	2.95	1.50	↓	188	.60	.40	↓	213	3.00	↓	↓
164	.03	2.00	↓	189	1.00	.20	↓	214	4.20	↓	↓
165	.60	↓	↓	190	↓	↓	1.20	215	5.60	↓	↓
166	1.80	↓	↓	191	↓	↓	2.40	216	5.90	↓	↓
167	2.95	↓	↓	192	↓	↓	3.60	217	.03	.90	↓
168	4.20	↓	↓	193	↓	↓	4.80	218	.03	↓	↓
169	5.40	↓	↓	194	↓	↓	6.00	219	1.40	↓	↓
170	.03	2.30	↓	195	2.00	.40	↓	220	3.00	↓	↓
171	2.95	2.30	↓	196	↓	↓	1.80	221	4.20	↓	↓
172	.03	.10	.10	197	↓	↓	3.00	222	5.60	↓	↓
173	↓	↓	.40	198	↓	↓	4.20	223	5.90	↓	↓
174	↓	↓	.60	199	↓	↓	5.40	224	.30	1.90	↓
175	↓	↓	1.20	200	↓	↓	6.00	225	3.00	1.90	↓

[a]See figure 7.

TABLE I. Concluded

Thermocouple	x, in. (a)	y, in. (a)	z, in. (a)	Thermocouple	x, in. (a)	y, in. (a)	z, in. (a)
226	5.60	1.90	6.44	242	5.90	0.20	0.20
227	5.90	.03	6.20	243	↓	.20	.10
228	↓	↓	4.80	244	↓	.20	.03
229	↓	↓	3.00	245	↓	.40	.40
230	↓	↓	1.60	246	↓	.40	.03
231	↓	↓	.60	247	↓	1.00	6.20
232	↓	↓	.40	248	↓	↓	4.80
233	↓	↓	.20	249	↓	↓	3.00
234	↓	↓	.03	250	↓	↓	1.60
235	↓	.10	.20	251	↓	↓	.40
236	↓	.10	.10	252	↓	↓	.03
237	↓	.20	6.20	253	↓	2.00	6.20
238	↓	↓	4.80	254	↓	↓	3.00
239	↓	↓	3.00	255	↓	↓	.40
240	↓	↓	1.60	256	↓	↓	.03
241	↓	↓	.60				

[a]See figure 7.

TABLE II. TUNNEL CONDITIONS AND TEST PARAMETERS FOR TILE ARRAY

Test	Type of flow	$T_{t,c}$, °R	q_∞, psia	α, deg	M	R	Panel-holder configuration (ref. 6)	Λ, deg	W, in.
1	Laminar	3090	2.17	0.3	3.2	2.01×10^6	Blunt	0	0.07
2	↓	3130	2.15	↓	3.2	2.06	↓	15	↓
3		3040	2.16		3.2	2.07		30	
4		3110	2.17		3.2	2.10		60	
5		3130	2.07		3.2	2.09		45	↓
6		3130	2.07		3.2	2.09		↓	.04
7		3180	2.18		3.2	1.98			.12
8	↓	3280	2.19		3.2	1.79	↓		.16
9	Turbulent	3320	2.22		3.2	1.92	Blunt, trips		.16
10	↓	3330	2.22		3.2	1.91	↓		.12
11		3350	2.15		3.2	1.85			.04
12		3320	2.22		3.2	1.92			.07
13		3340	2.18		3.2	1.88		60	↓
14		3360	2.10		3.2	1.87		30	
15		3410	2.29		3.2	1.77		15	
16		3250	2.20	↓	3.2	1.86	↓	0	
17		3080	3.48	7.6	5.5	5.01	Sharp, trips	↓	
18		3110	8.74	↓	5.4	11.70	↓		
[a]19		3380	3.54		5.6	4.50			
20		3260	3.64		5.6	4.83		15	
21		3260	3.61		5.6	4.79		30	
22		3320	3.49		5.7	4.70		60	
23		3190	3.42		5.6	4.80		45	↓
24		3140	3.32	↓	5.6	4.81		45	.04
25		3350	3.57	7.5	5.6	4.59		0	.07
26	↓	3170	9.03	.3	6.5	7.67	↓	45	.07

[a]Nominal step height of 0.035 in.

TABLE III. TOTAL HEAT LOADS AND FLAT-PLATE HEATING RATE

Test	Q, Btu/sec	Q_{top}, Btu/sec	$Q_{side\ 1}$, Btu/sec	$Q_{side\ 2}$, Btu/sec	$Q_{side\ 3}$, Btu/sec	$Q_{side\ 4}$, Btu/sec	Q_{FP}, Btu/sec	$\dot{q}_{FP,corr}$, Btu/ft^2-sec
1	0.175	0.130	0.014	0.011	0.006	0.014	0.102	0.393
2	.224	.176	.013	.010	.011	.013	.107	.410
3	.222	.161	.020	.015	.009	.017	.100	.385
4	.323	.257	.025	.013	.008	.020	.103	.397
5	.194	.153	.010	.013	.009	.010	.106	.406
6	.259	.204	.018	.012	.009	.016	.106	.406
7	.173	.118	.016	.013	.010	.017	.110	.422
8	.216	.167	.016	.009	.010	.014	.116	.447
9	.376	.283	.032	.016	.013	.033	.437	1.681
10	.484	.386	.027	.019	.026	.025	.439	1.688
11	.465	.369	.028	.031	.012	.025	.442	1.701
12	.423	.350	.027	.021	.011	.015	.440	1.692
13	.351	.293	.025	.010	.009	.015	.441	1.696
14	.414	.331	.027	.024	.015	.017	.447	1.718
15	.485	.393	.034	.023	.012	.023	.454	1.746
16	.350	.194	.054	.039	.017	.046	.424	1.632
17	2.771	2.231	.201	.103	.069	.166	1.257	4.835
18	4.682	3.687	.422	.200	.147	.227	2.976	11.446
19	2.349	1.850	.232	.083	.047	.137	1.438	5.532
20	2.197	1.834	.086	.111	.031	.136	1.366	5.254
21	1.855	1.586	.058	.081	.028	.101	1.368	5.260
22	1.931	1.740	.074	.043	.041	.033	1.406	5.407
23	1.876	1.708	.056	.051	.030	.033	1.326	5.099
24	1.963	1.790	.050	.055	.027	.041	1.296	4.986
25	2.726	2.171	.134	.153	.072	.196	1.428	5.491
26	2.204	1.834	.106	.085	.050	.129	1.513	5.818

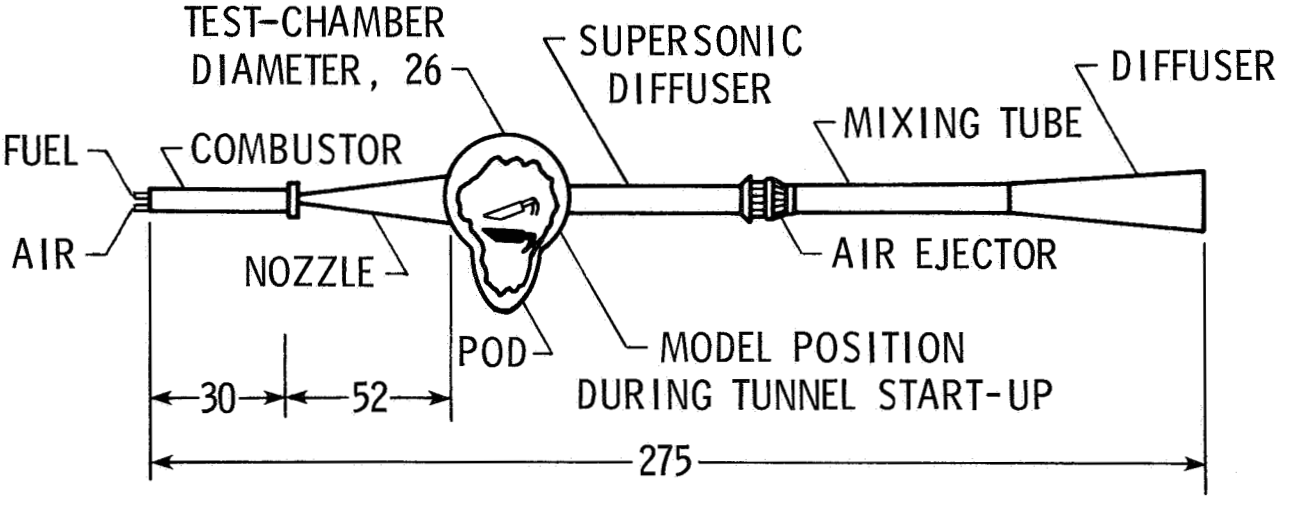

Figure 1. The Langley 8-Foot High-Temperature Tunnel. Dimensions are given in feet.

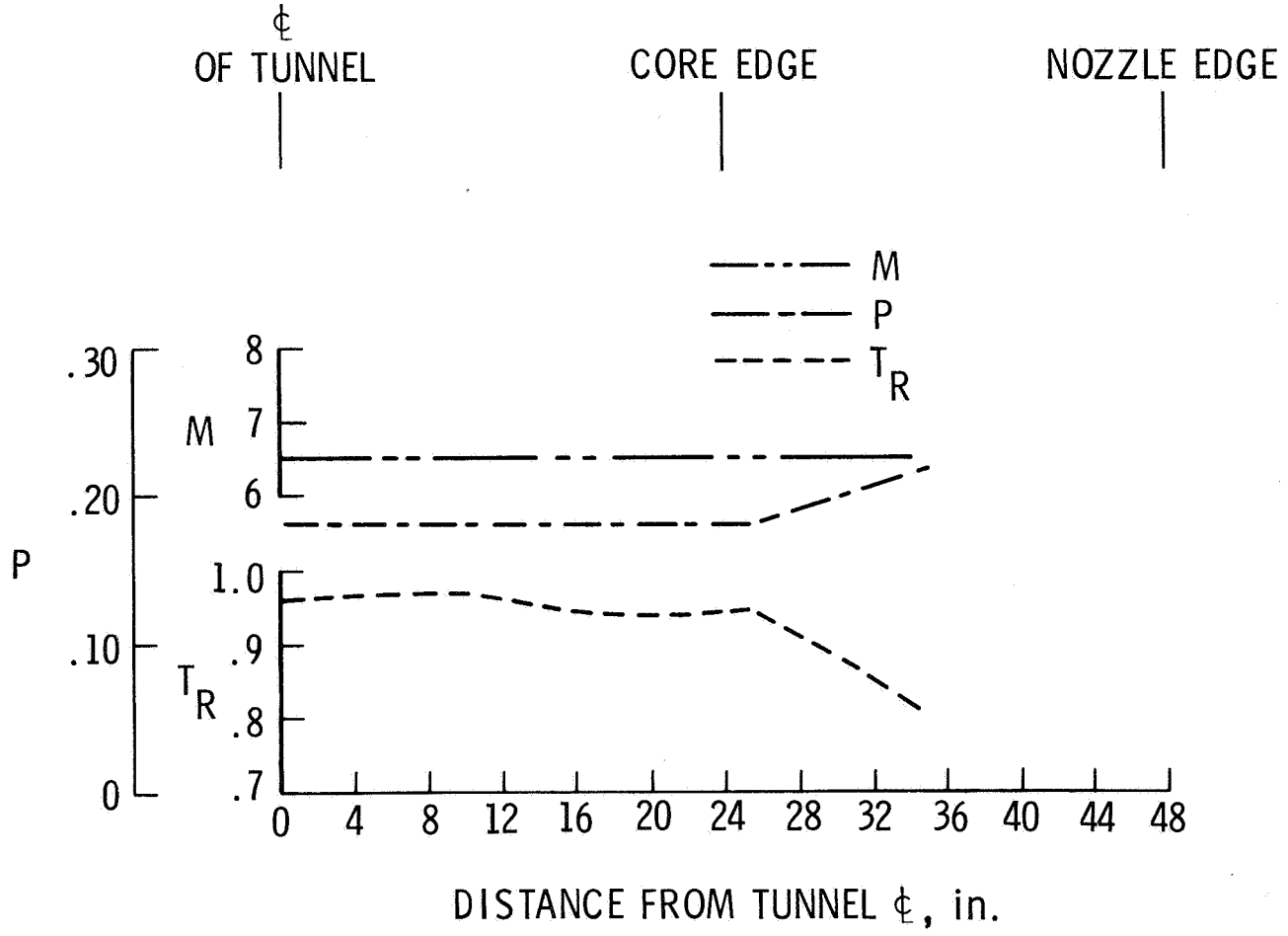

Figure 2. Extent of core flow uniformity in the Langley 8-Foot High-Temperature Tunnel. Total pressure in combustor, 1025 psia; $T_{t,c} = 3000°R$.

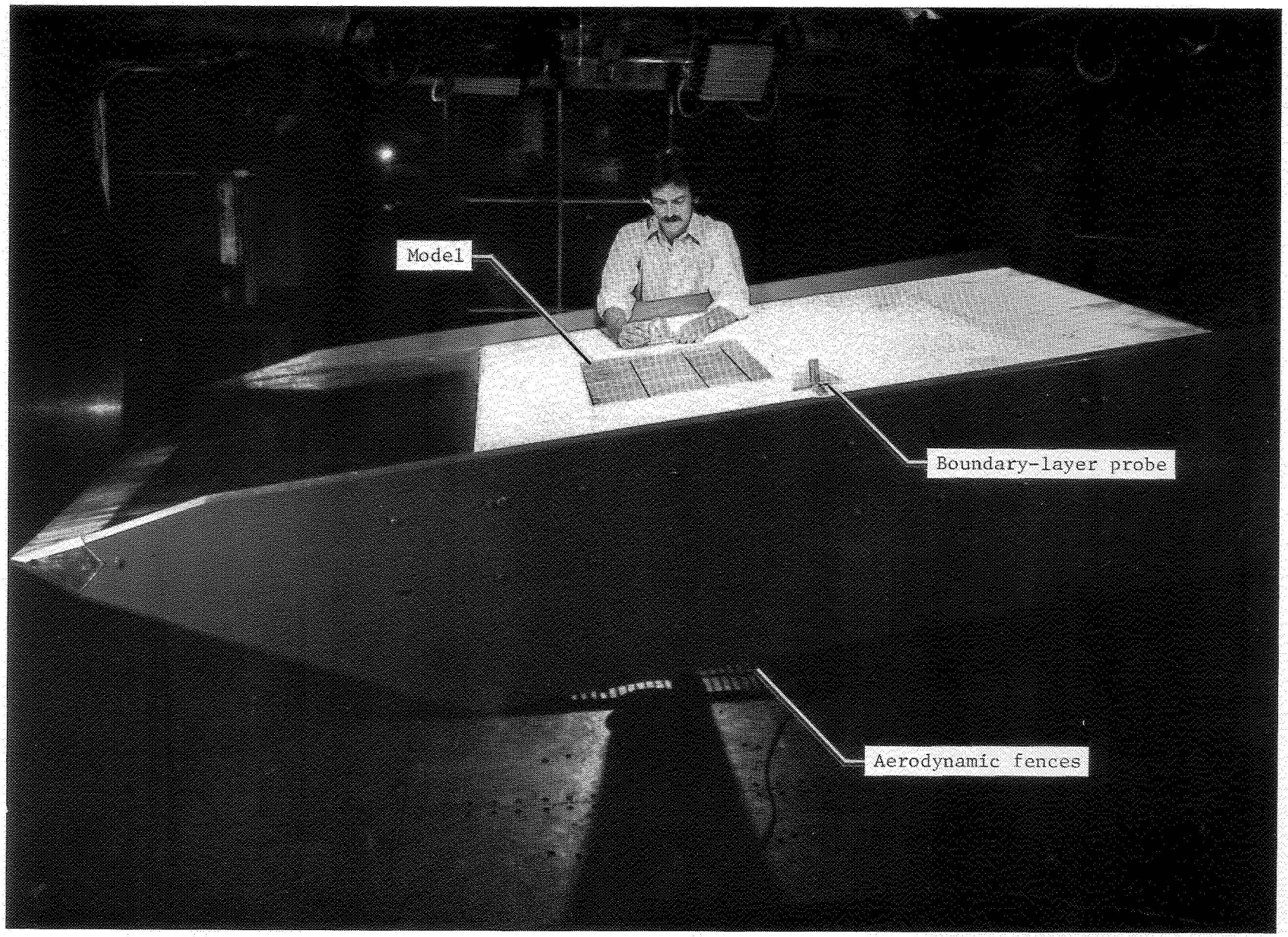

L-81-6357

Figure 3. Panel holder with gap heating model installed in the Langley 8-Foot High-Temperature Tunnel.

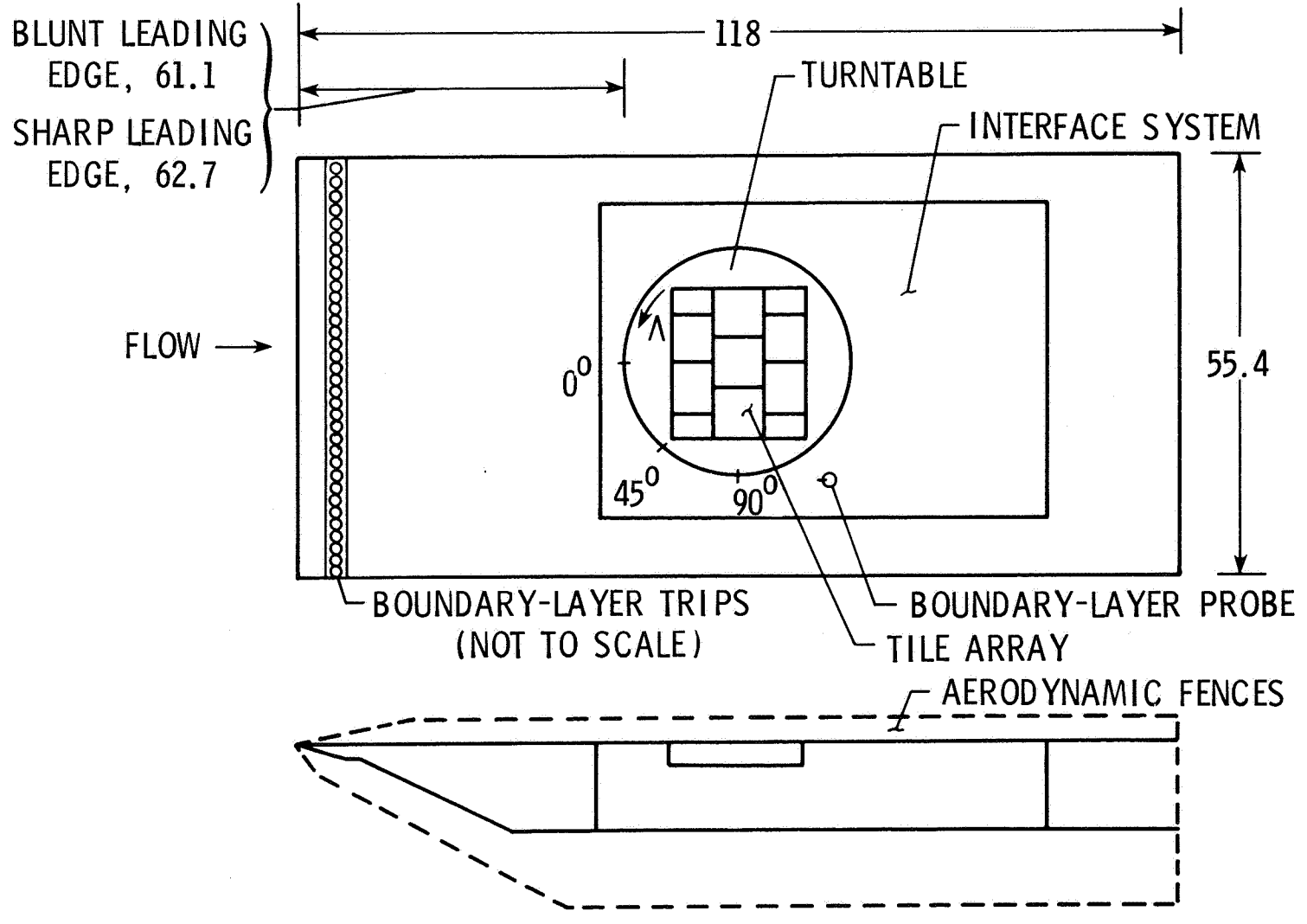

Figure 4. Sharp leading-edge panel holder with model installed at $\Lambda = 0°$. Dimensions are given in inches unless otherwise specified.

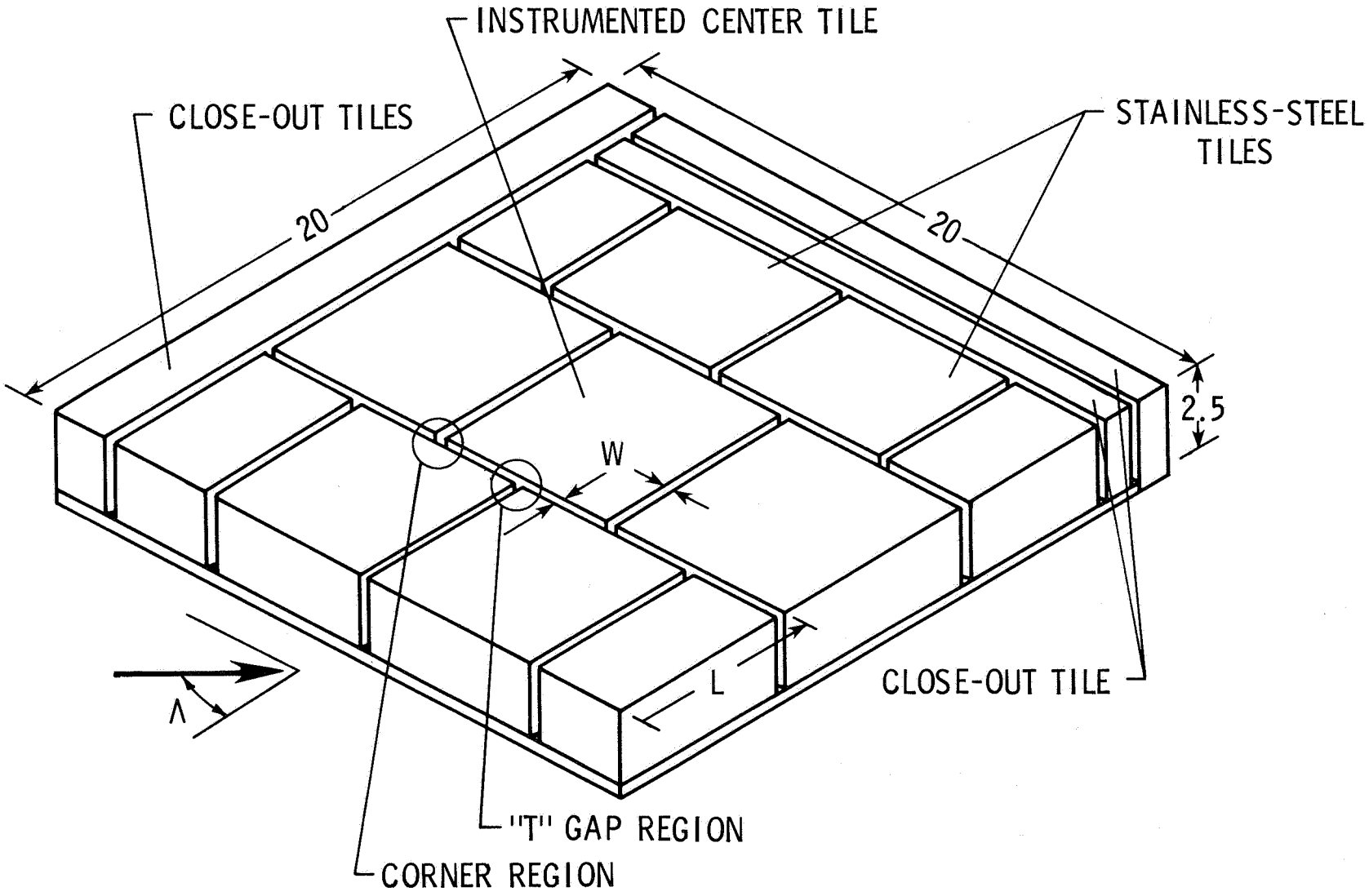

Figure 5. Metallic tile array and test parameters. Dimensions are given in inches unless otherwise specified.

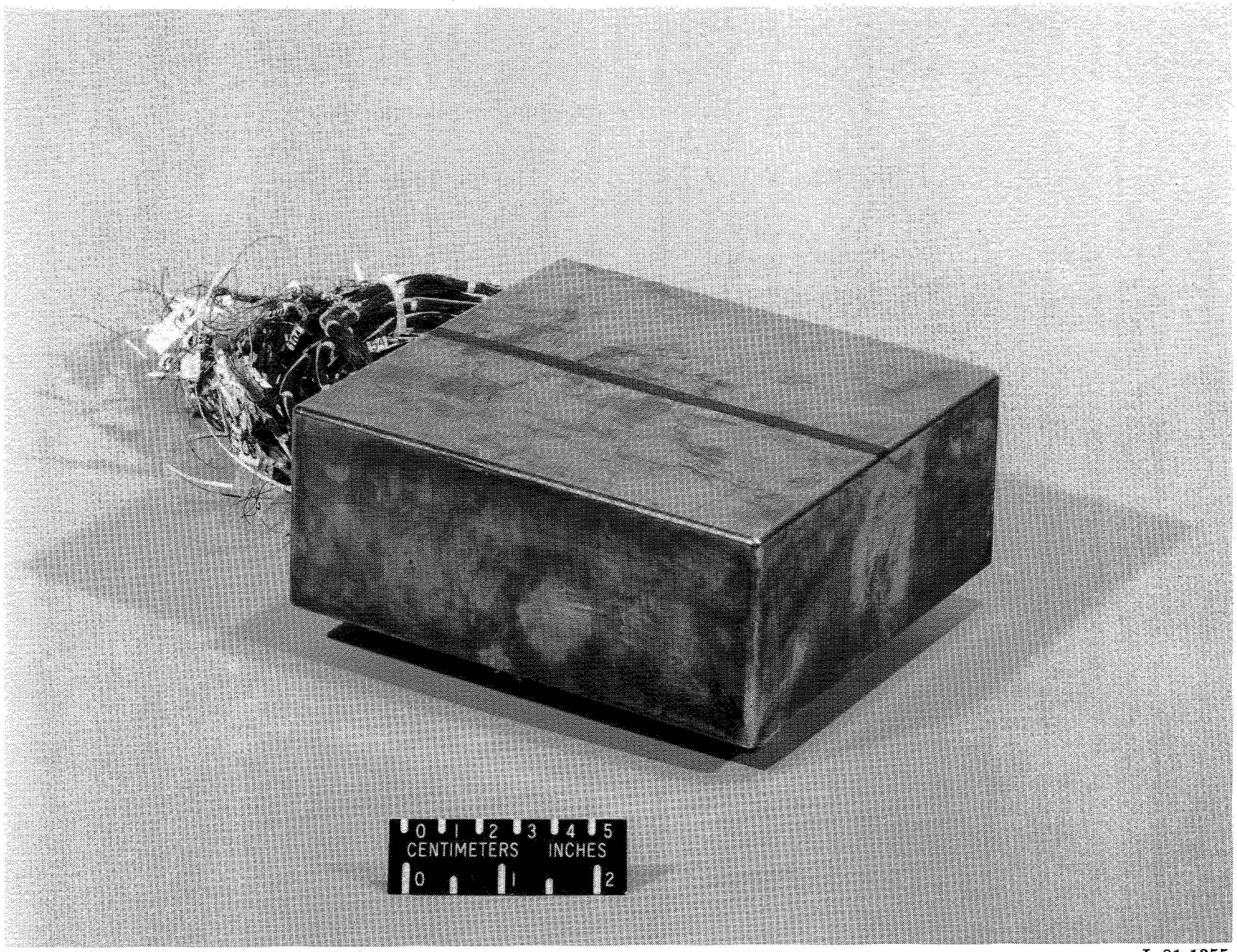

L-81-1355

Figure 6. Niculoy 22 gap heating tile.

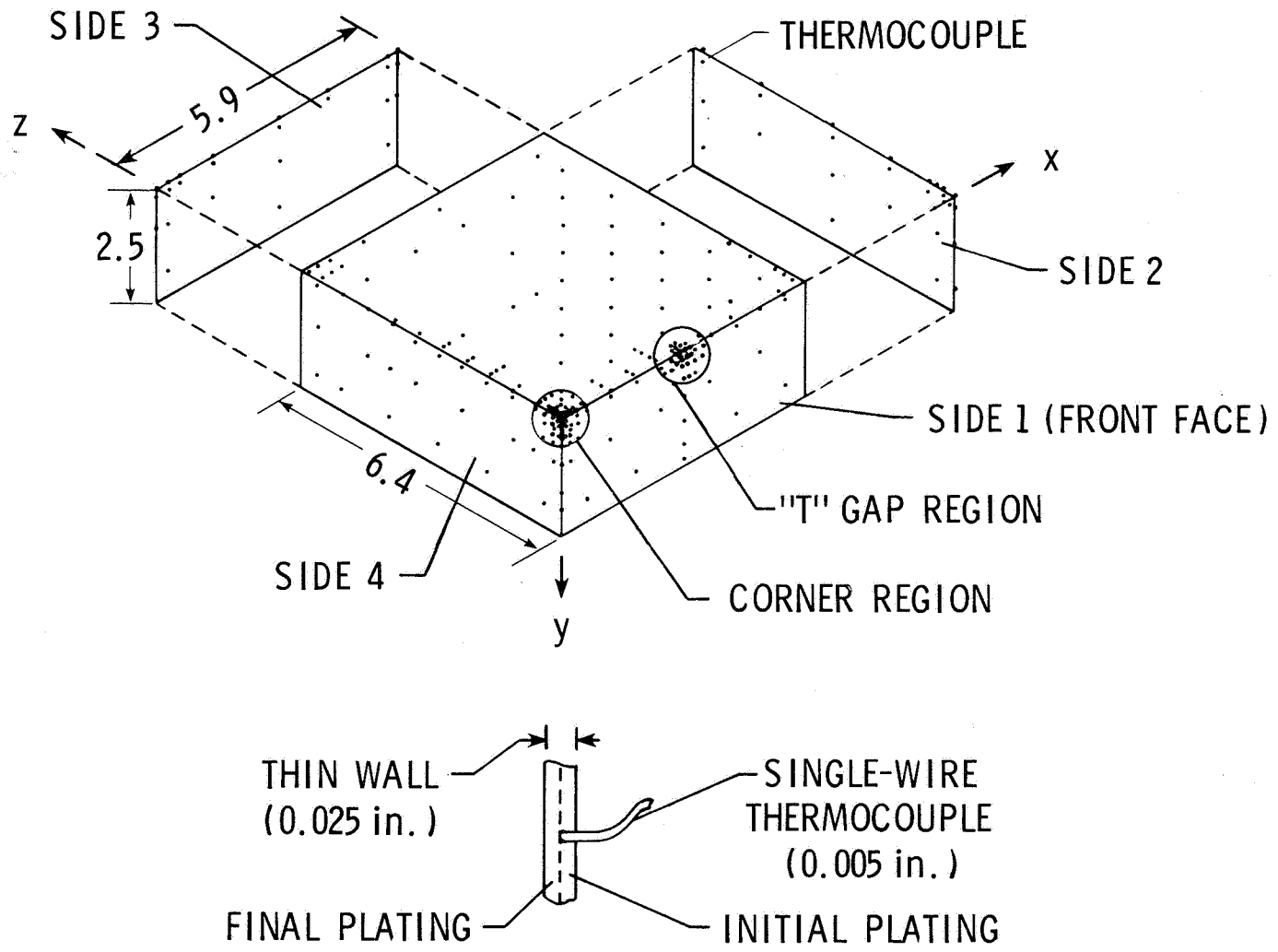

Figure 7. Instrumented center tile and instrumentation detail. Dimensions are given in inches.

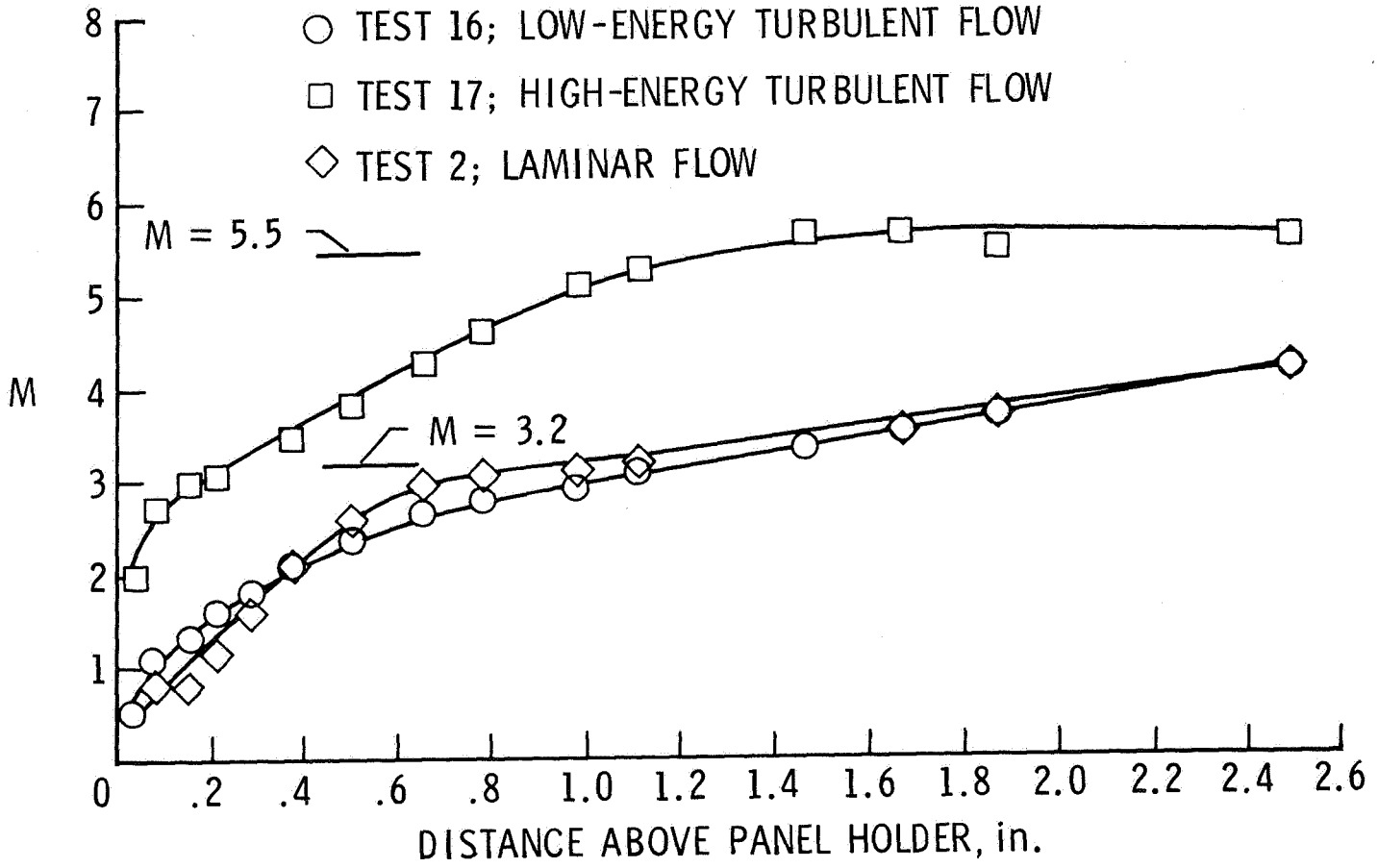

Figure 8. Typical Mach number profile through boundary layer on panel holder for three tests.

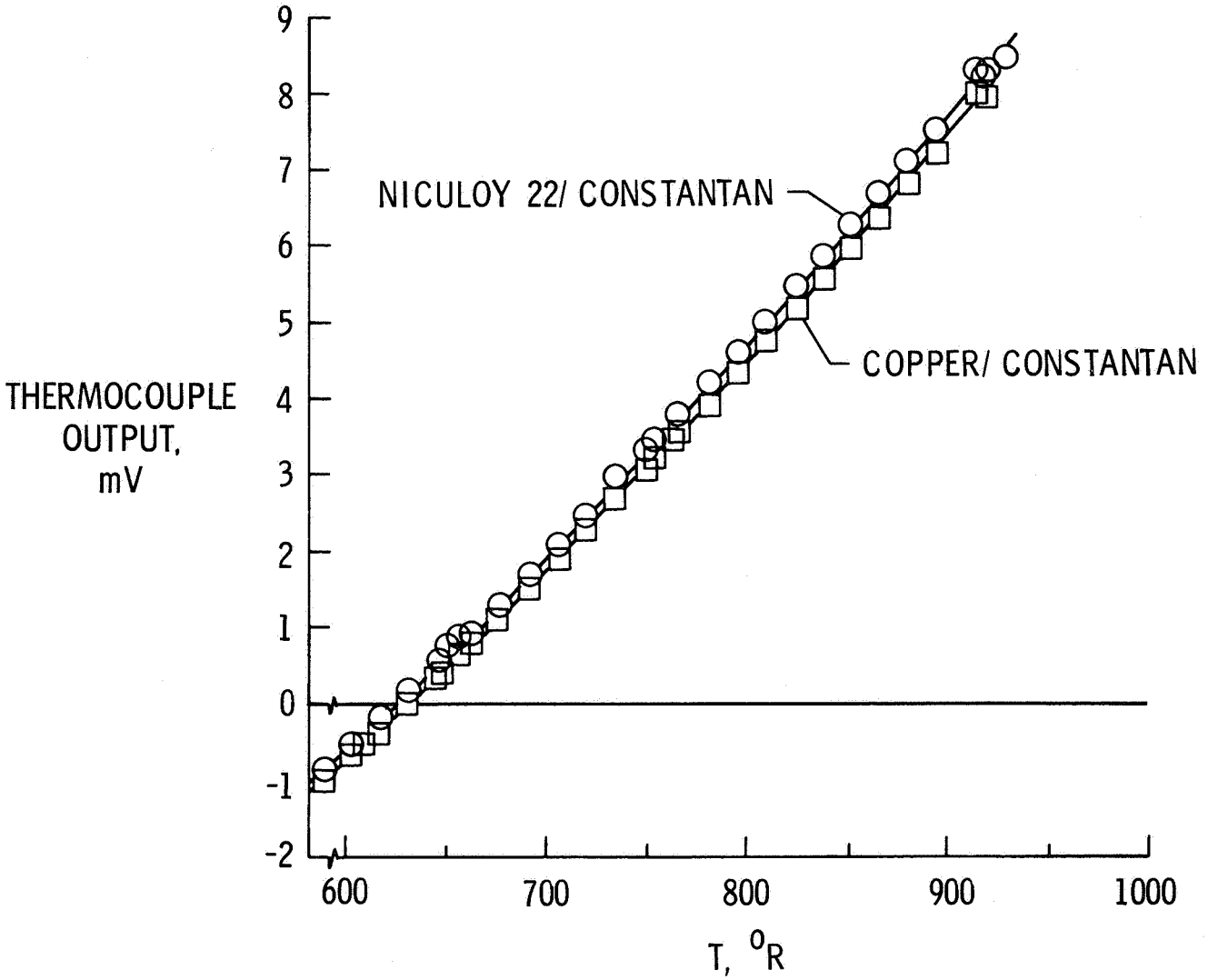

Figure 9. Comparison of calibrations for Niculoy 22/constantan and copper/constantan thermocouples.

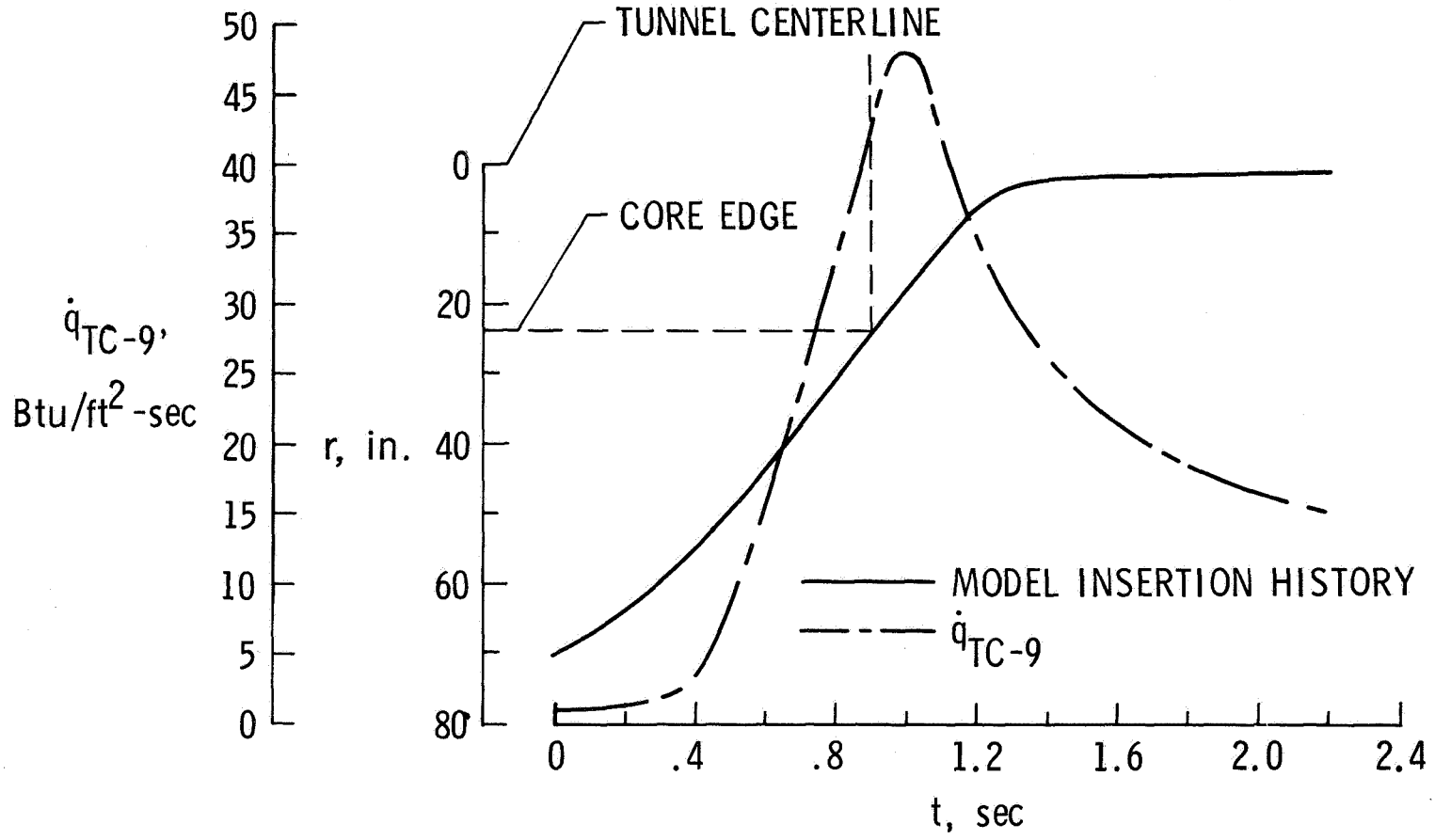

Figure 10. Typical history of events during model insertion into test stream.

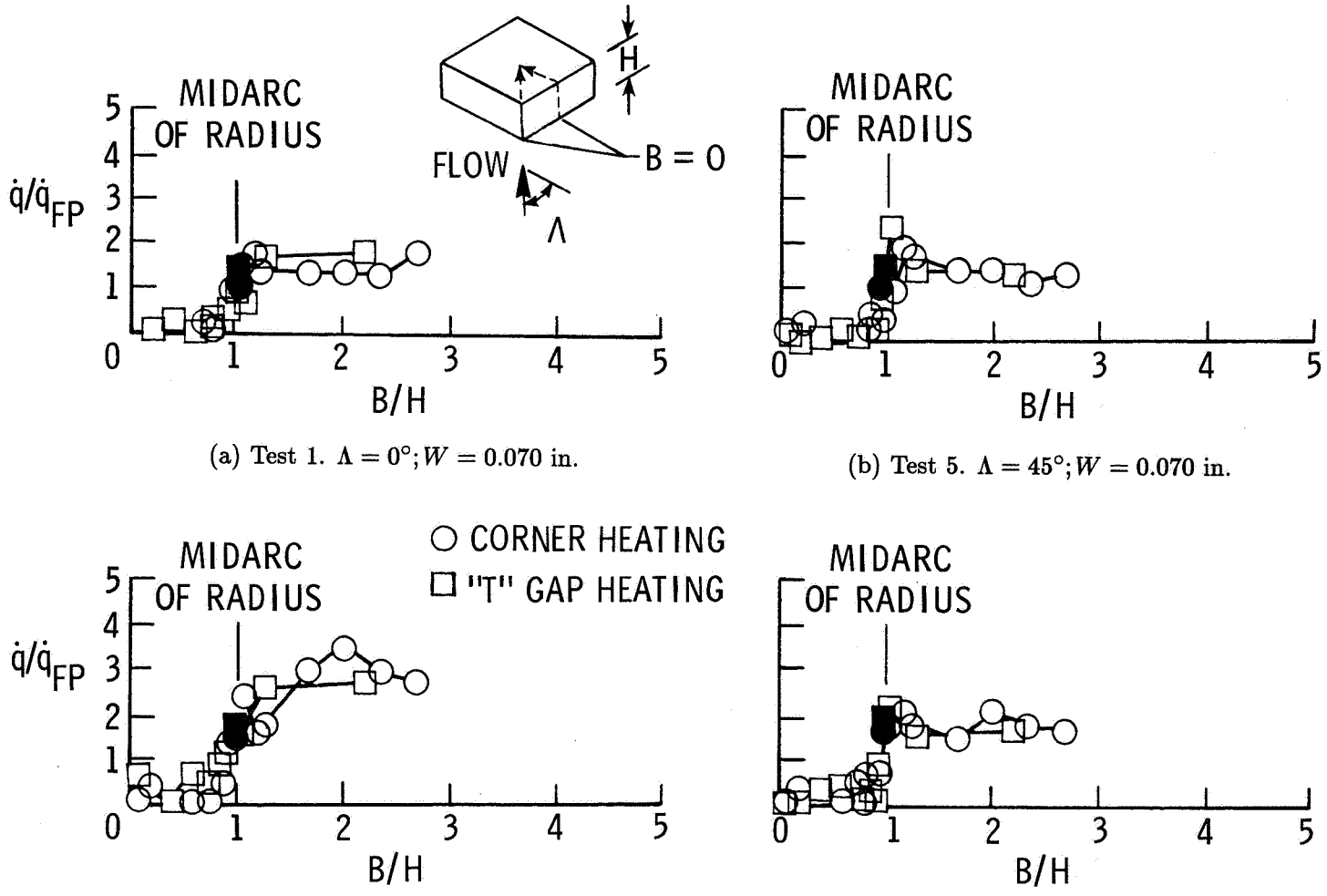

(a) Test 1. $\Lambda = 0°; W = 0.070$ in.

(b) Test 5. $\Lambda = 45°; W = 0.070$ in.

(c) Test 4. $\Lambda = 60°; W = 0.070$ in.

(d) Test 8. $\Lambda = 45°; W = 0.160$ in.

Figure 11. Heating distributions in flow impingement regions for laminar flow. Solid symbols denote TC-1 and TC-9.

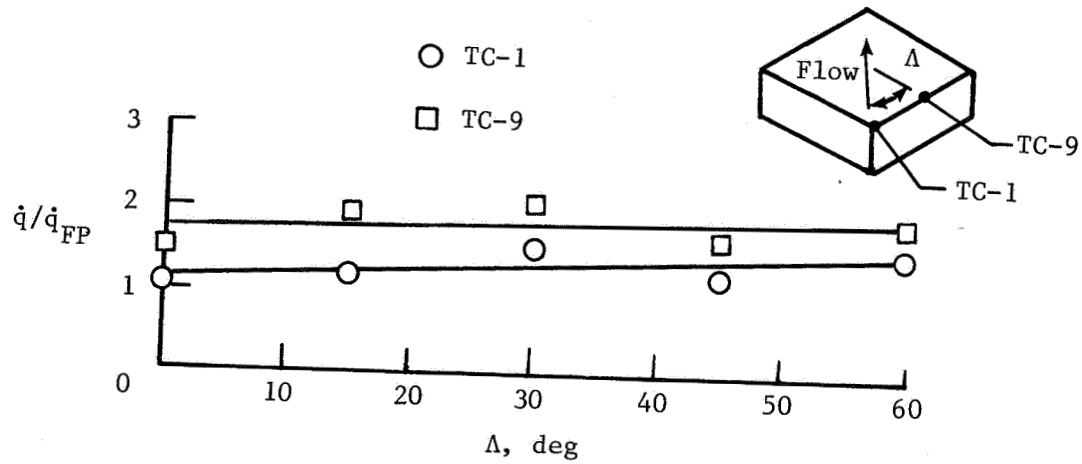

Figure 12. Effect of flow angularity on corner and "T" gap heating in laminar flow. $W = 0.070$ in.

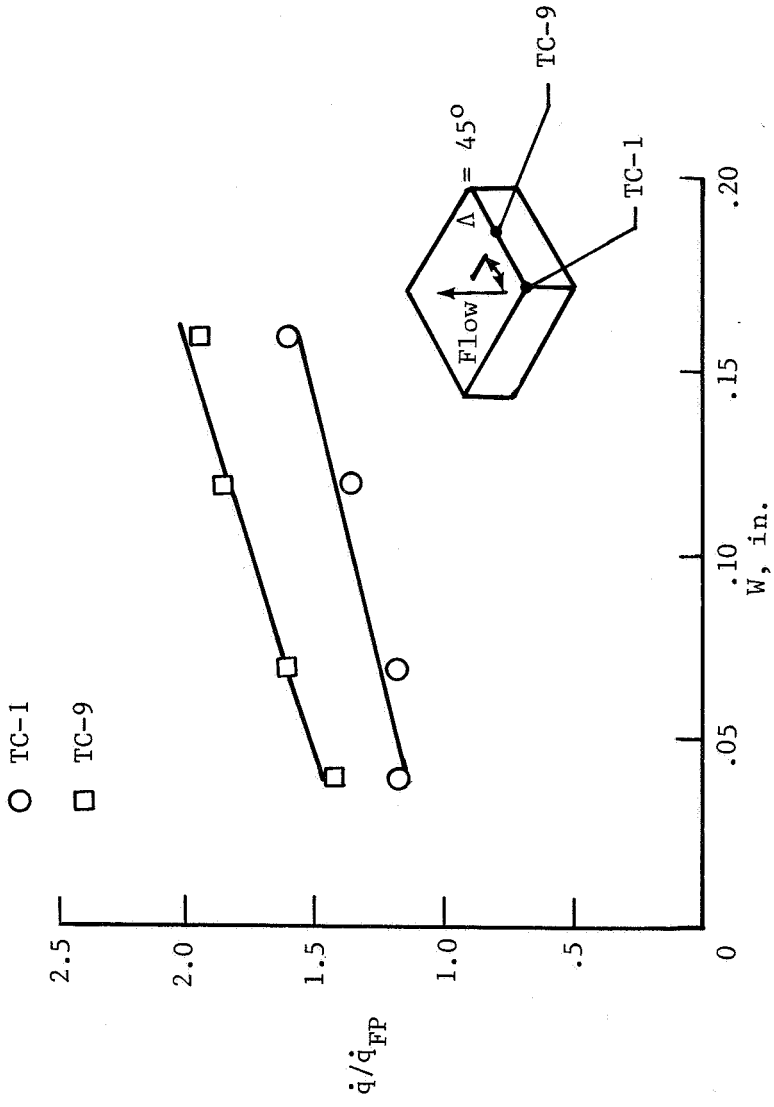

Figure 13. Effect of gap width on corner and "T" gap heating in laminar flow.

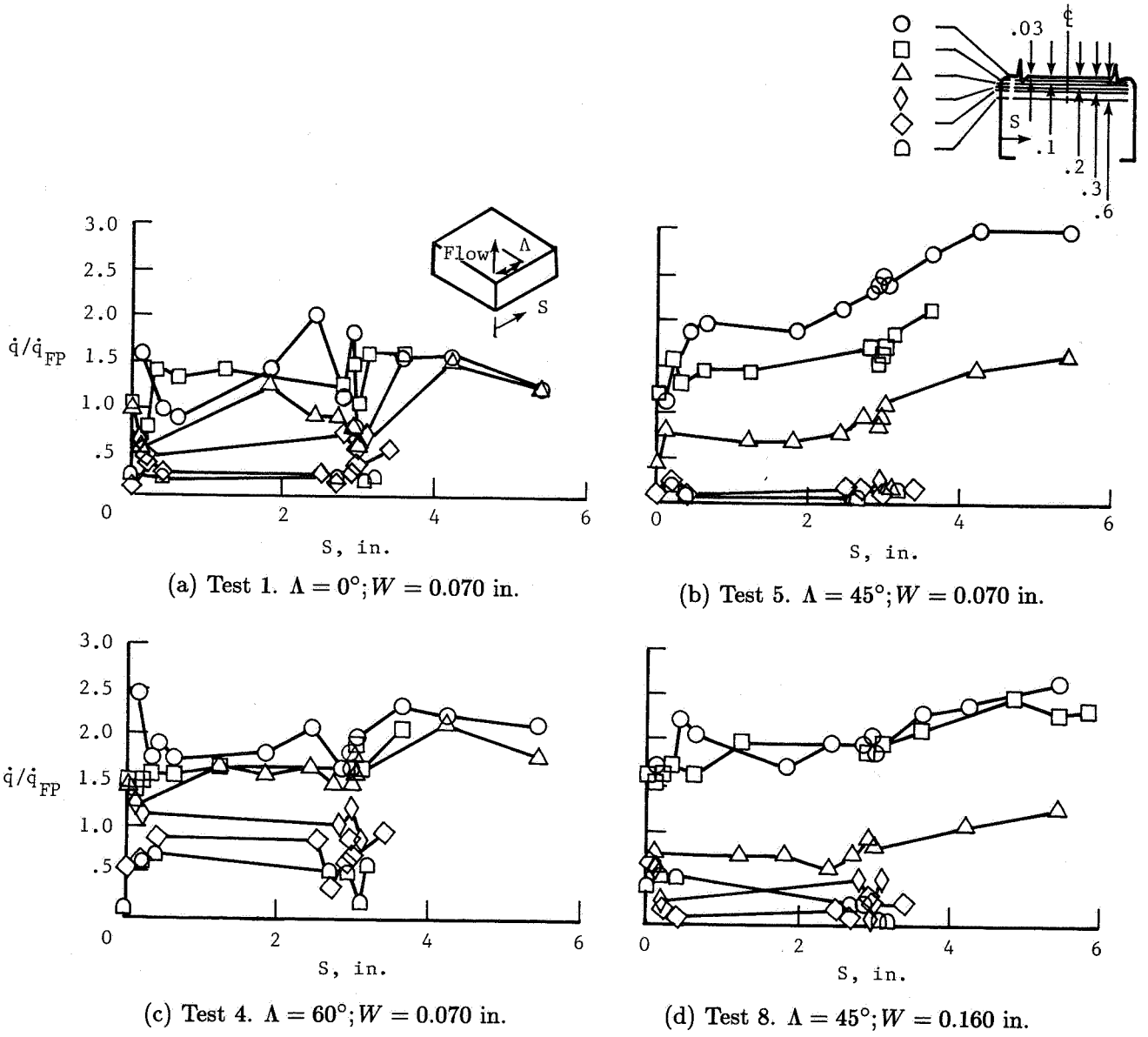

(a) Test 1. $\Lambda = 0°; W = 0.070$ in.

(b) Test 5. $\Lambda = 45°; W = 0.070$ in.

(c) Test 4. $\Lambda = 60°; W = 0.070$ in.

(d) Test 8. $\Lambda = 45°; W = 0.160$ in.

Figure 14. Heating distributions on front face (side 1) of tile for laminar flow. Dimensions are given in inches unless otherwise specified.

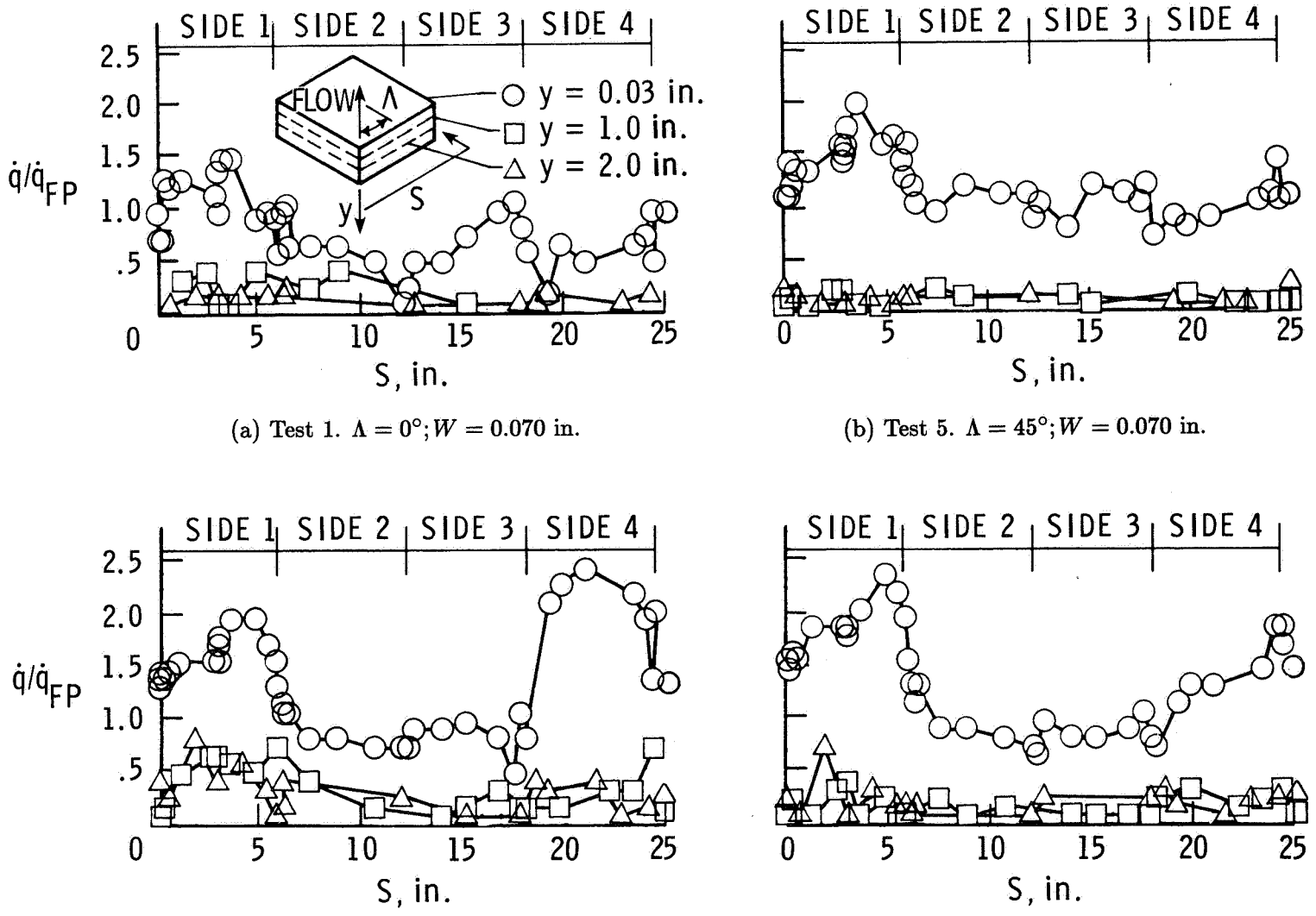

(a) Test 1. $\Lambda = 0°; W = 0.070$ in.

(b) Test 5. $\Lambda = 45°; W = 0.070$ in.

(c) Test 4. $\Lambda = 60°; W = 0.070$ in.

(d) Test 8. $\Lambda = 45°; W = 0.160$ in.

Figure 15. Heating distributions around sides of tile for laminar flow.

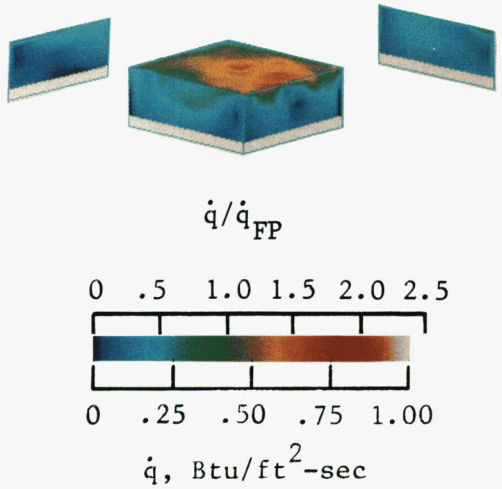

(a) Test 1. $\Lambda = 0°; W = 0.070$ in.

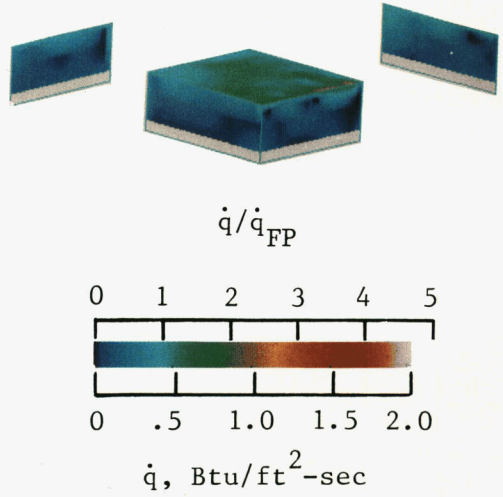

(b) Test 5. $\Lambda = 45°; W = 0.070$ in.

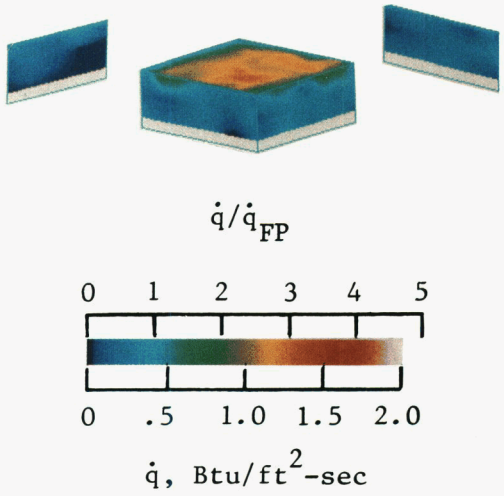

(c) Test 4. $\Lambda = 60°; W = 0.070$ in.

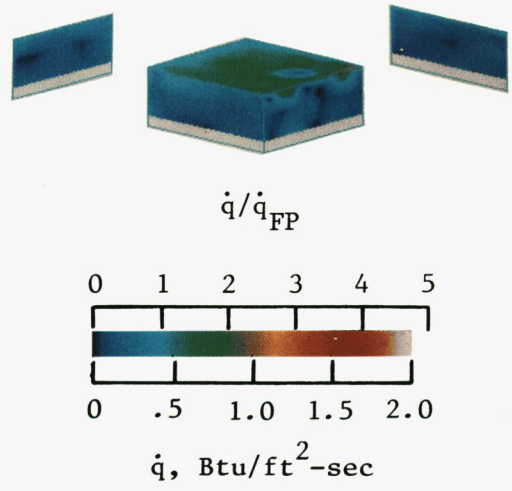

(d) Test 8. $\Lambda = 45°; W = 0.160$ in.

Figure 16. Overall heating distributions in laminar flow.

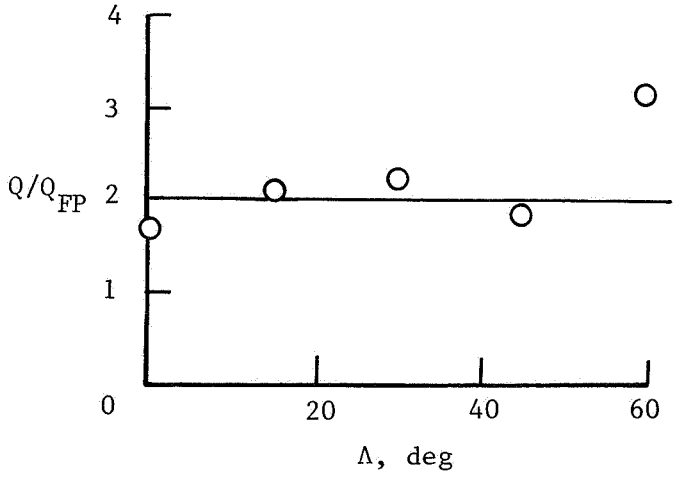

Figure 17. Effect of flow angularity on total heat load in laminar flow. $W = 0.070$ in.

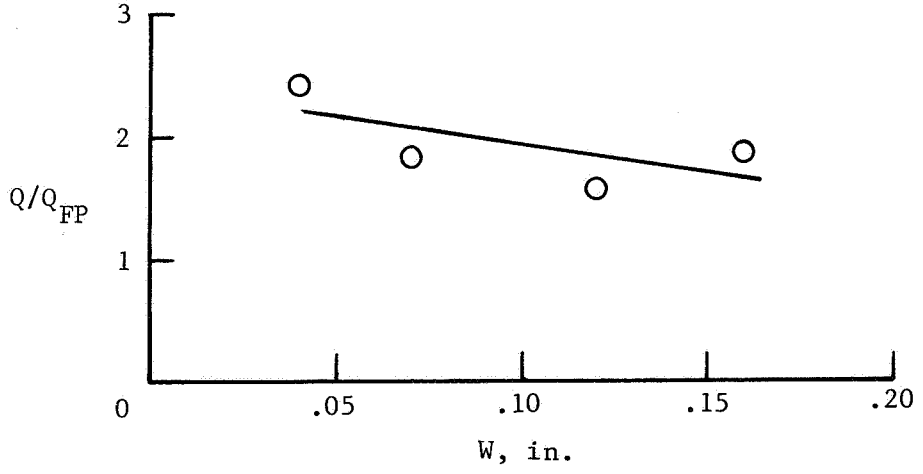

Figure 18. Effect of gap width on total heat load in laminar flow. $\Lambda = 45°$.

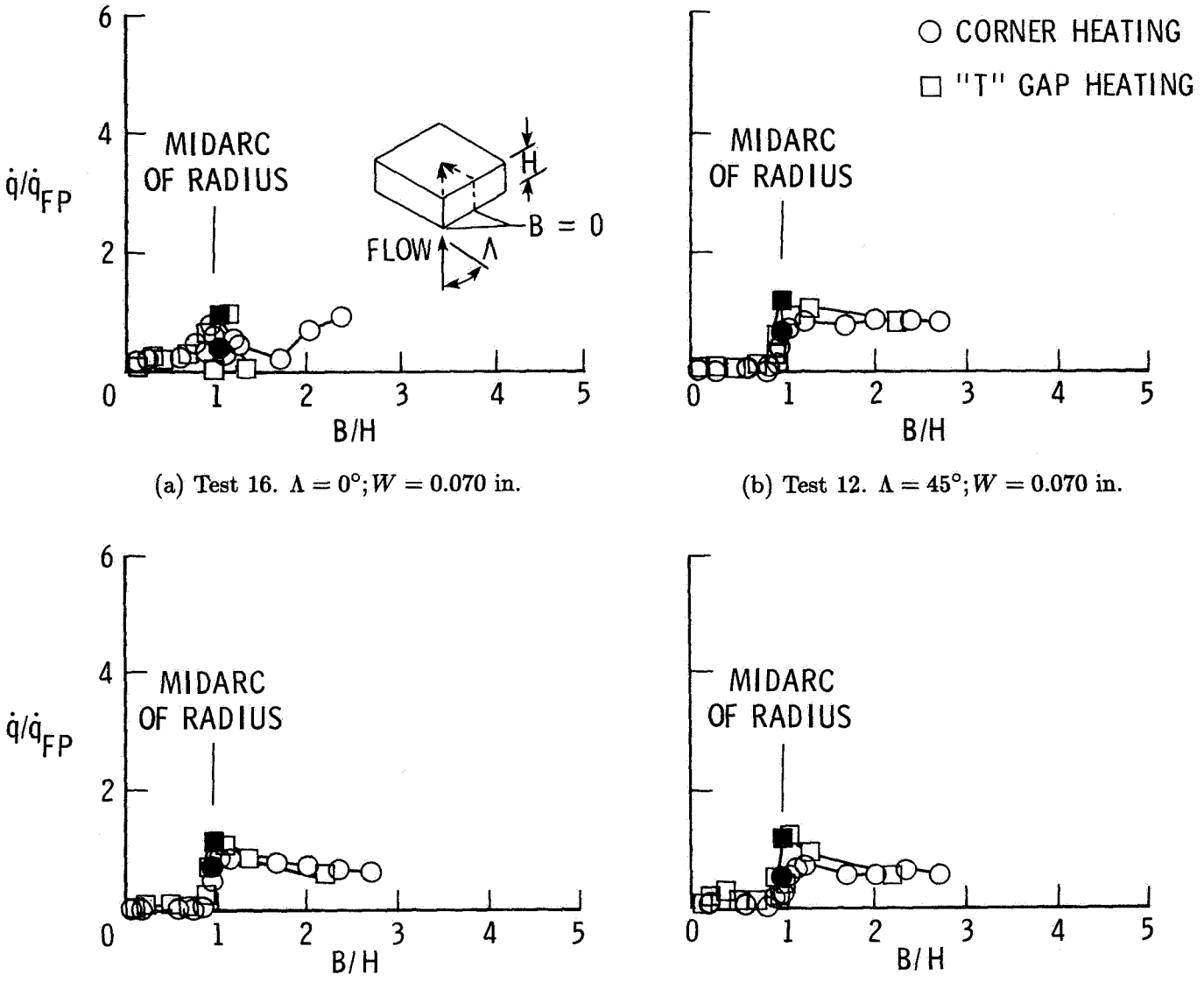

(a) Test 16. $\Lambda = 0°; W = 0.070$ in.

(b) Test 12. $\Lambda = 45°; W = 0.070$ in.

(c) Test 13. $\Lambda = 60°; W = 0.070$ in.

(d) Test 9. $\Lambda = 45°; W = 0.160$ in.

Figure 19. Characterization of heating in flow impingement regions for low-energy turbulent flow. Solid symbols denote TC-1 and TC-9.

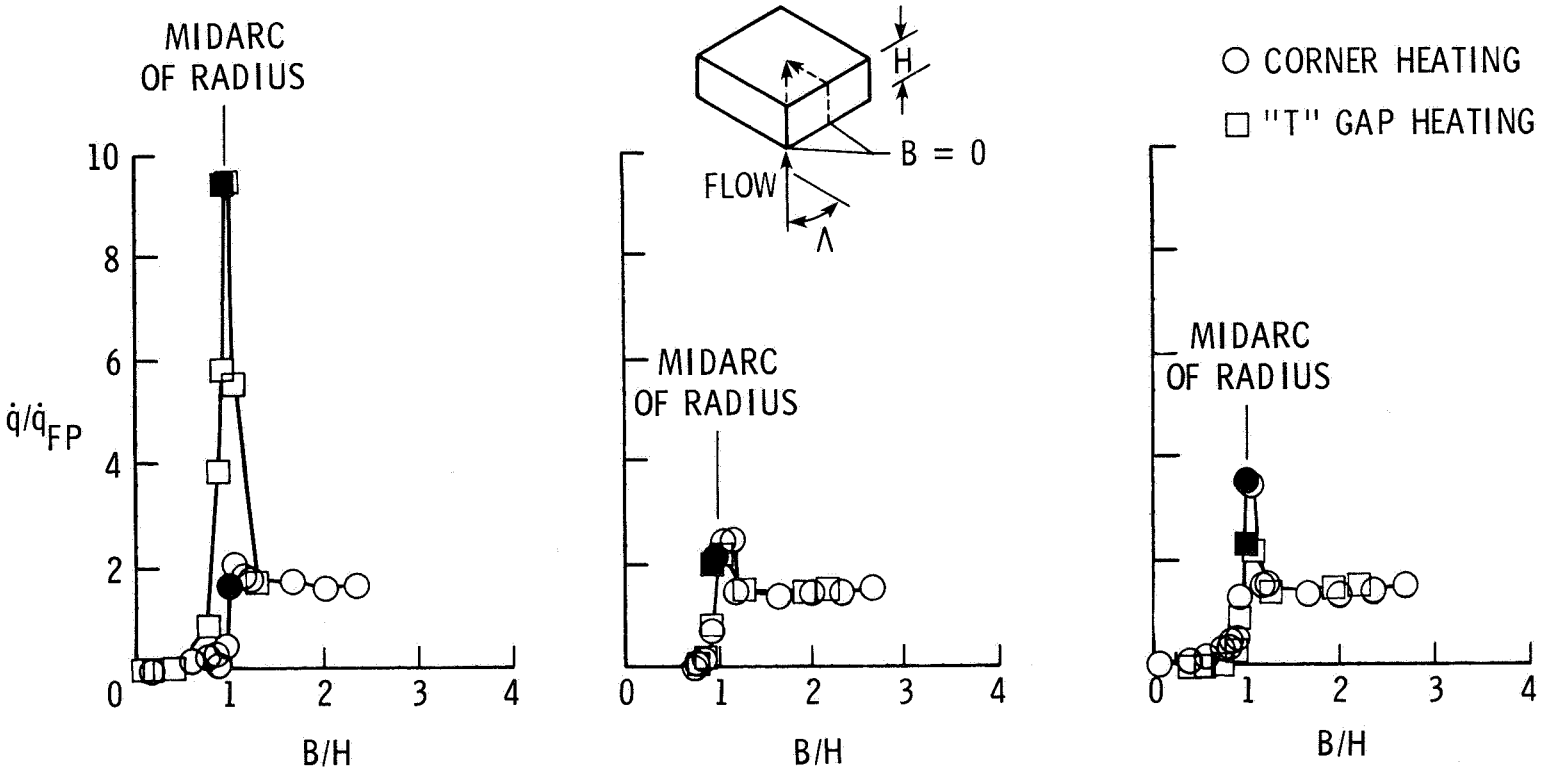

(a) Test 17. $\Lambda = 0°$.

(b) Test 23. $\Lambda = 45°$.

(c) Test 22. $\Lambda = 60°$.

Figure 20. Characterization of heating in flow impingement regions for high-energy turbulent flow. $W = 0.070$ in. Solid symbols denote TC-1 and TC-9.

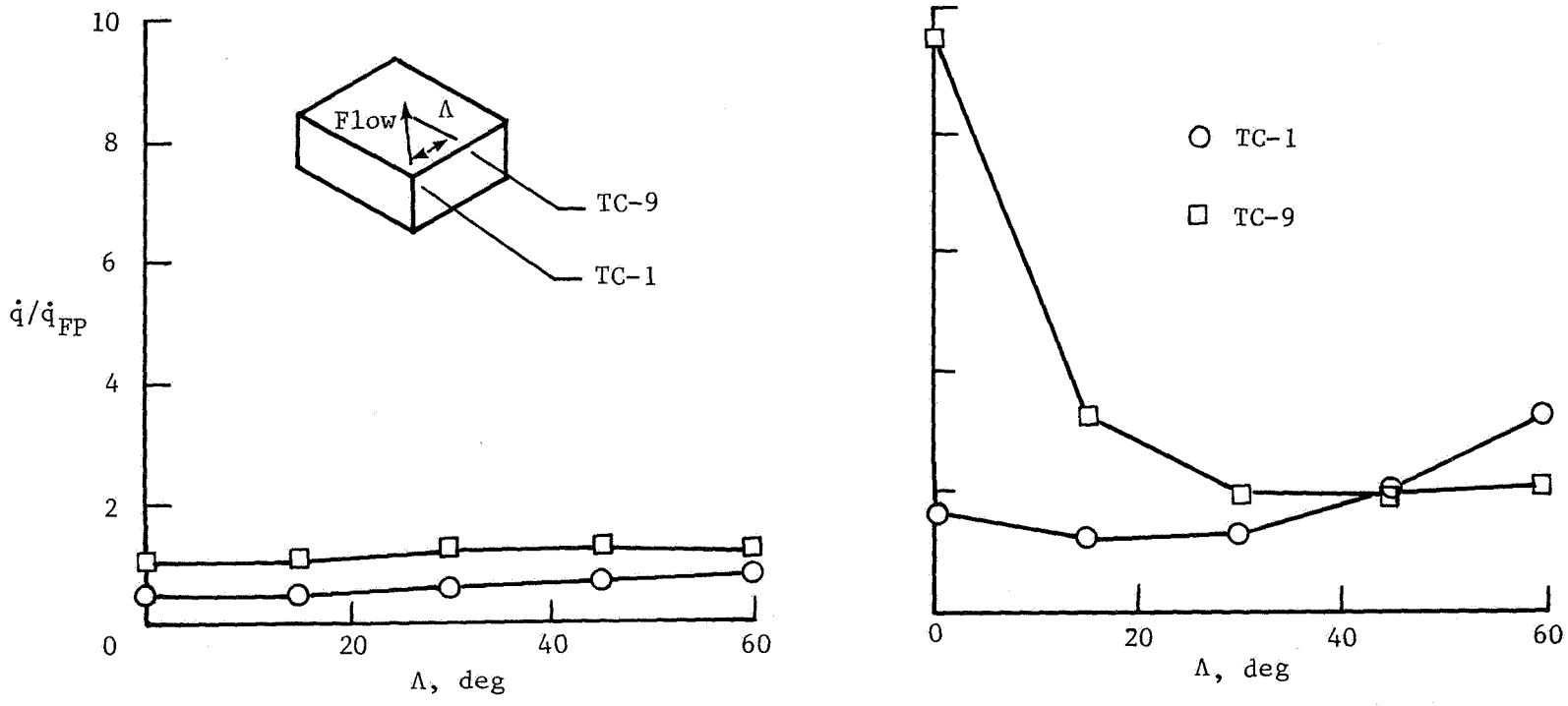

(a) Low-energy turbulent flow.

(b) High-energy turbulent flow.

Figure 21. Effect of flow angularity on corner and "T" gap heating in turbulent flow. $W = 0.070$ in.

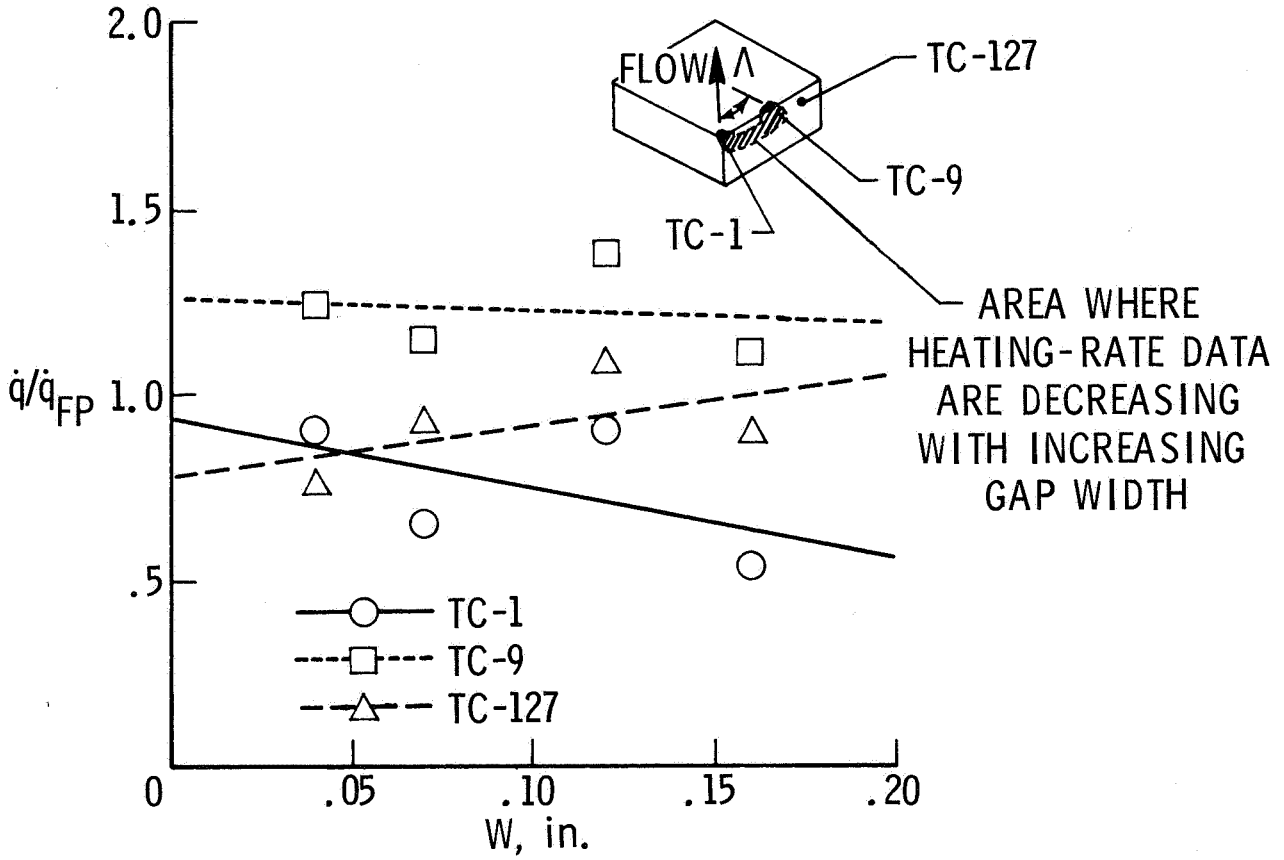

Figure 22. Effect of gap width on tile heating for low-energy turbulent flow. $\Lambda = 45°$.

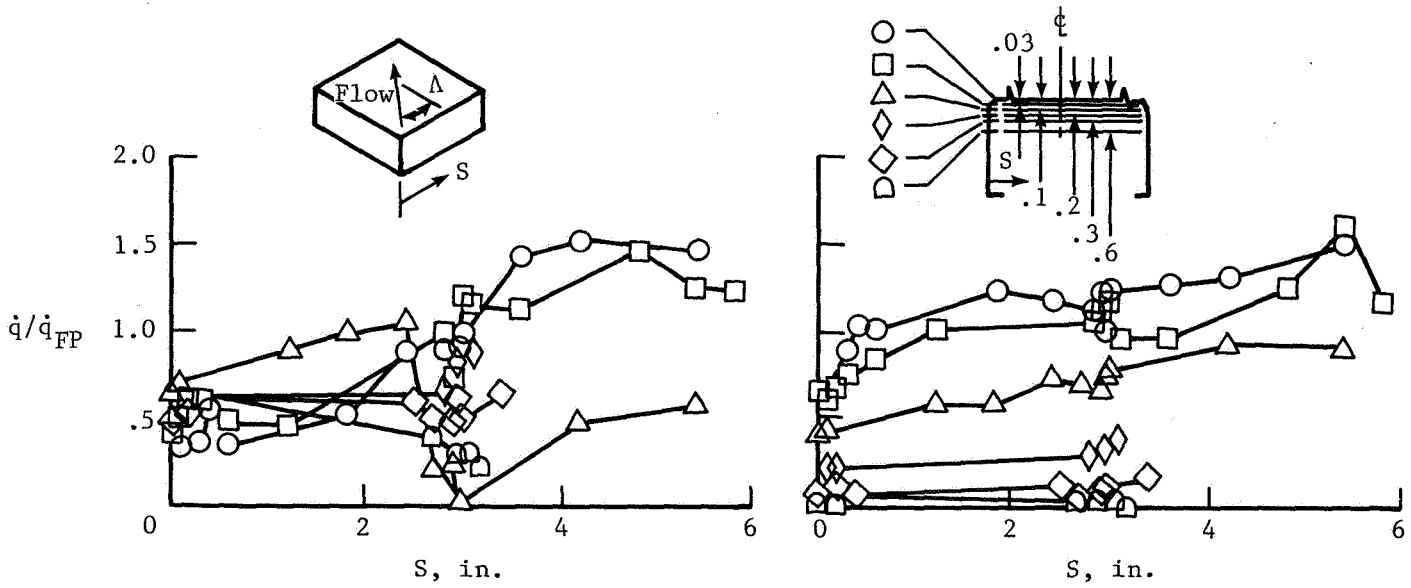

(a) Test 16. $\Lambda = 0°; W = 0.070$ in.

(b) Test 12. $\Lambda = 45°; W = 0.070$ in.

(c) Test 13. $\Lambda = 60°; W = 0.070$ in.

(d) Test 9. $\Lambda = 45°; W = 0.160$ in.

Figure 23. Front face (side 1) heating distribution for low-energy turbulent flow. Dimensions are given in inches unless otherwise specified.

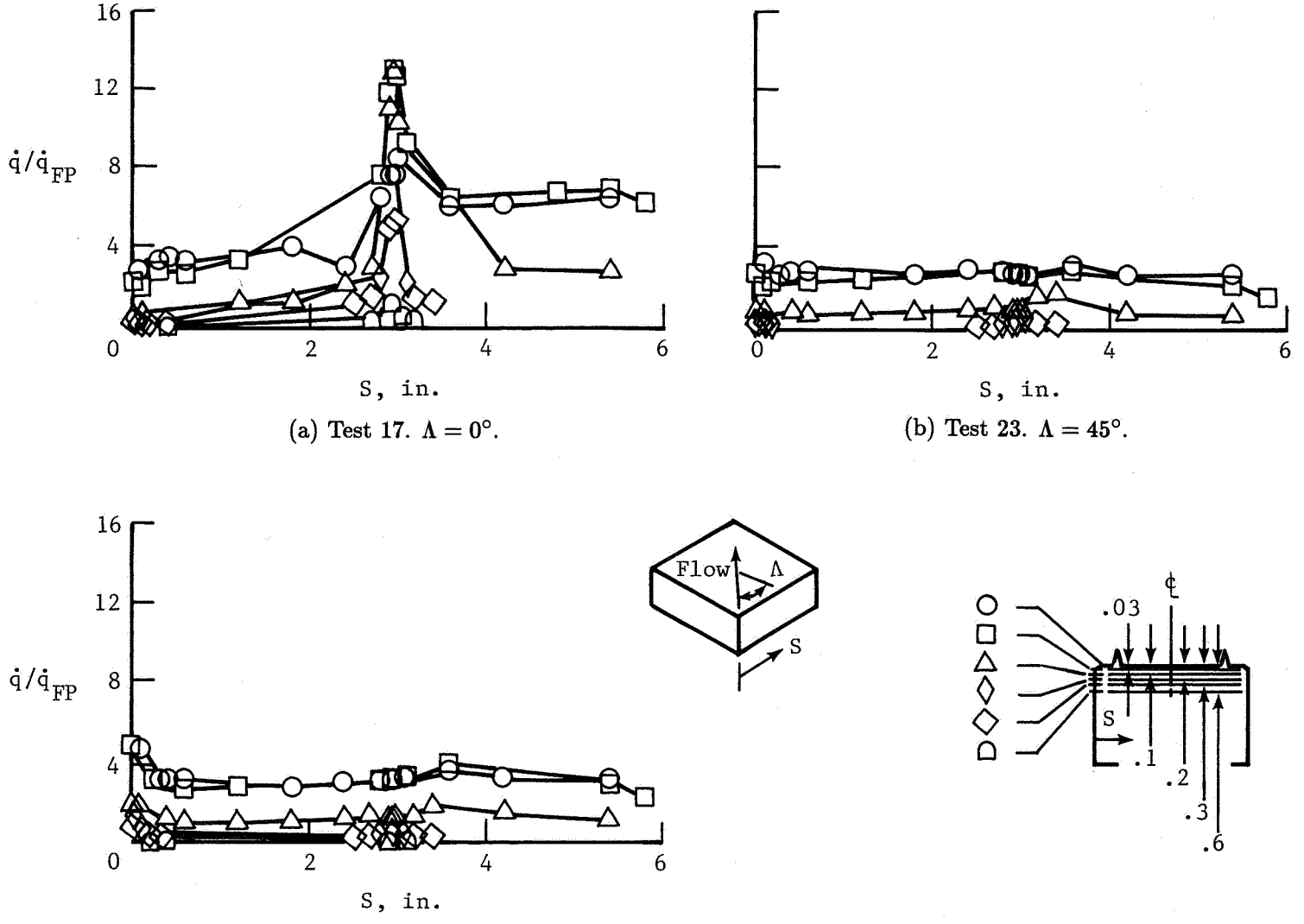

(a) Test 17. $\Lambda = 0°$.

(b) Test 23. $\Lambda = 45°$.

(c) Test 22. $\Lambda = 60°$.

Figure 24. Front face (side 1) heating distribution for high-energy turbulent flow. $W = 0.070$ in. Dimensions are given in inches unless otherwise specified.

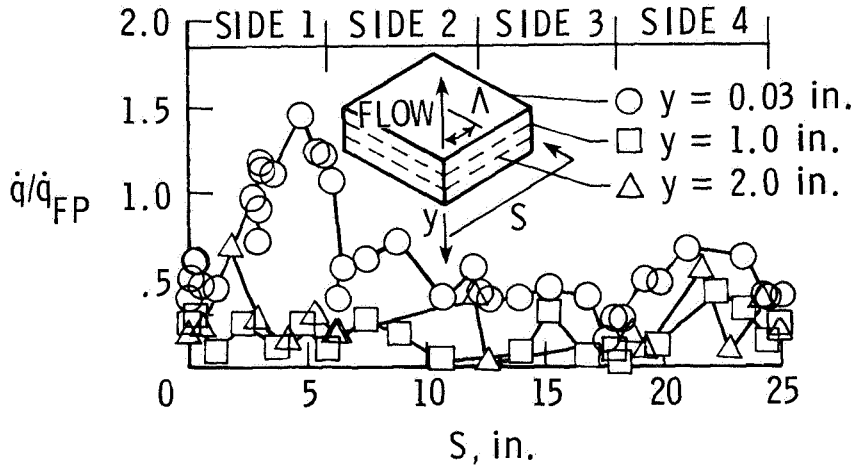

(a) Test 16. $\Lambda = 0°; W = 0.070$ in.

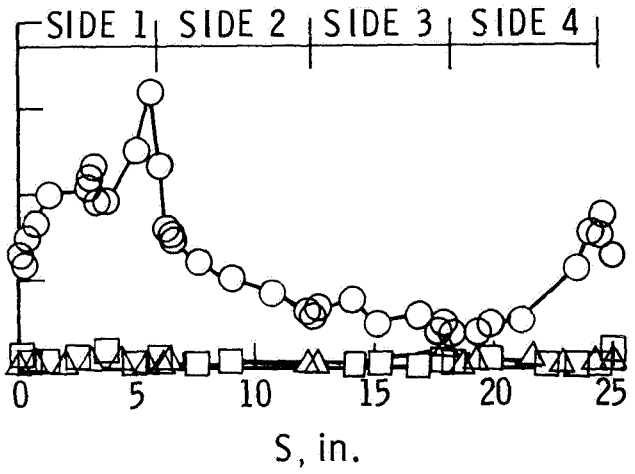

(b) Test 12. $\Lambda = 45°; W = 0.070$ in.

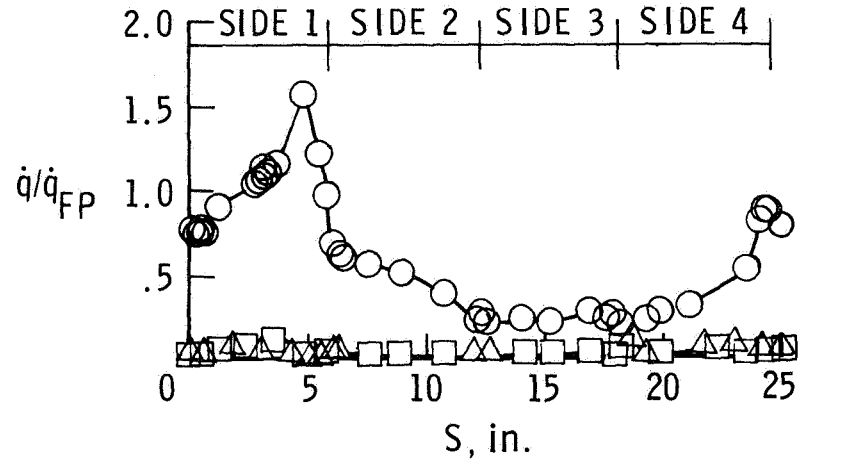

(c) Test 13. $\Lambda = 60°; W = 0.070$ in.

(d) Test 9. $\Lambda = 45°; W = 0.160$ in.

Figure 25. Heating distribution around sides of tile for low-energy turbulent flow.

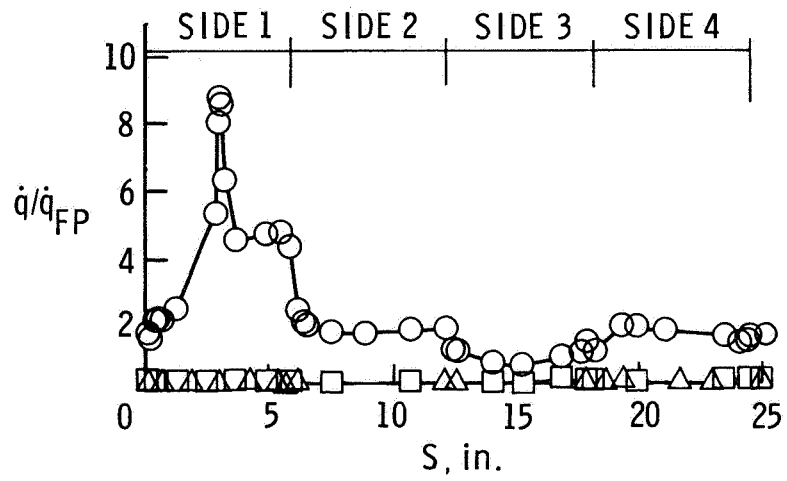

(a) Test 17. $\Lambda = 0°$.

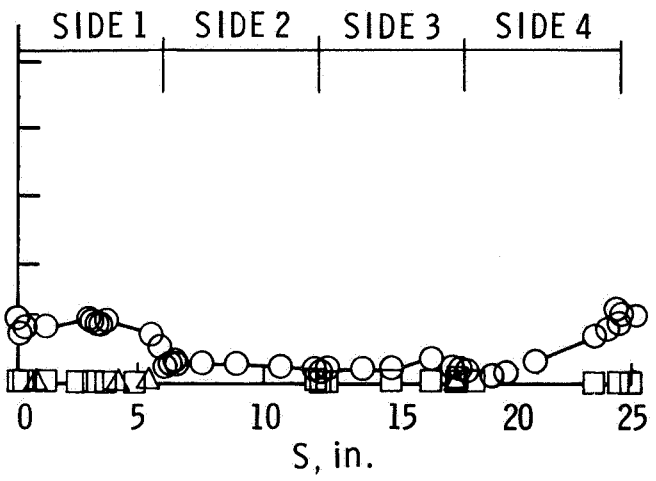

(b) Test 23. $\Lambda = 45°$.

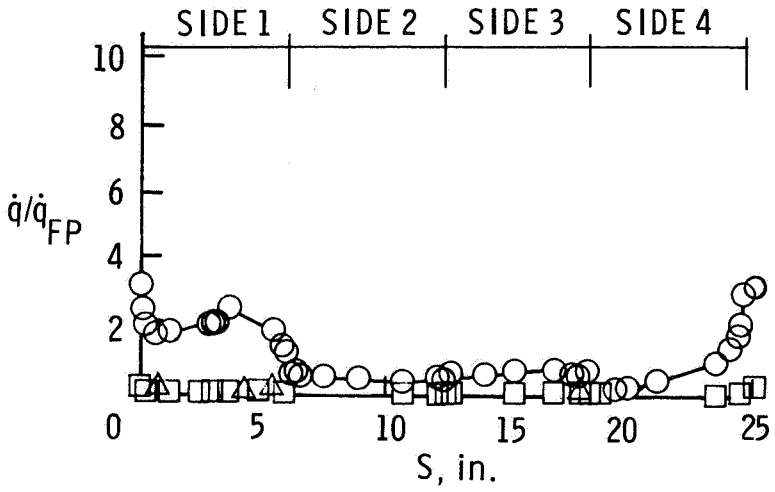

(c) Test 22. $\Lambda = 60°$.

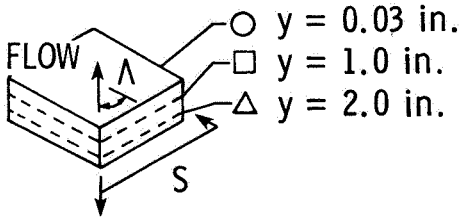

Figure 26. Heating distribution around sides of tile for high-energy turbulent flow. $W = 0.070$ in.

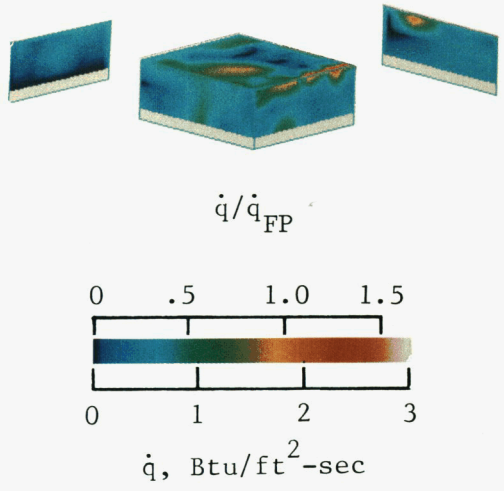

(a) Test 16. $\Lambda = 0°; W = 0.070$ in.

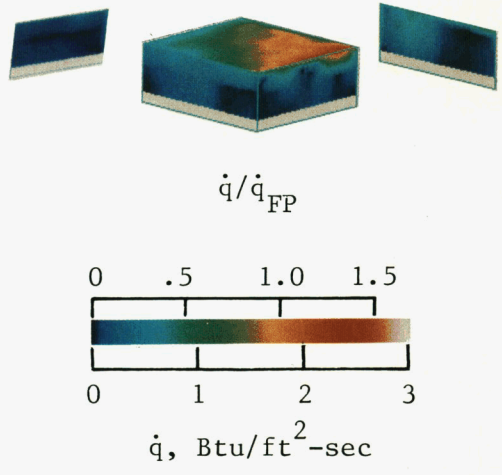

(b) Test 12. $\Lambda = 45°; W = 0.070$ in.

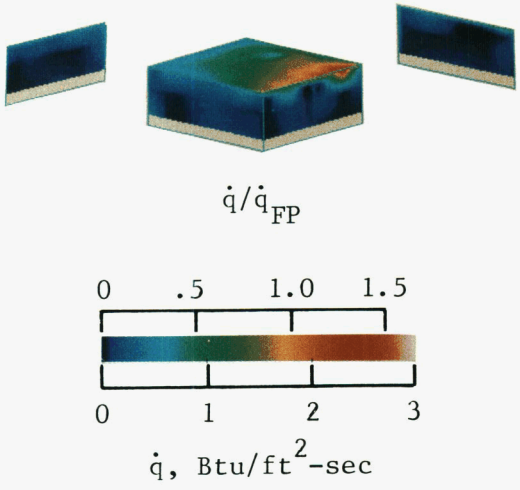

(c) Test 13. $\Lambda = 60°; W = 0.070$ in.

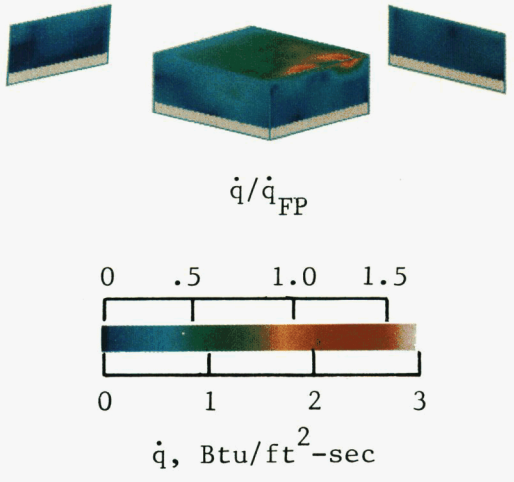

(d) Test 9. $\Lambda = 45°; W = 0.160$ in.

Figure 27. Overall heating distributions in low-energy turbulent flow.

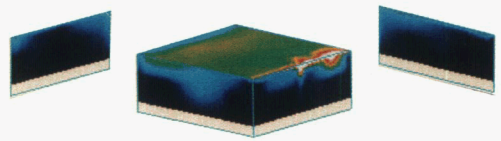

$\dot{q}/\dot{q}_{FP}$

0 2 4 6 8 10

0 10 20 30 40 50

$\dot{q}$, Btu/ft^2-sec

(a) Test 17. $\Lambda = 0°$.

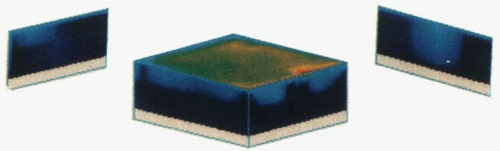

$\dot{q}/\dot{q}_{FP}$

0 1 2 3

0 3 6 9 12 15

$\dot{q}$, Btu/ft^2-sec

(b) Test 23. $\Lambda = 45°$.

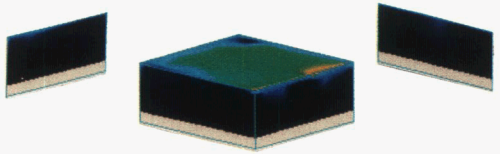

$\dot{q}/\dot{q}_{FP}$

0 1 2 3

0 4 8 12 16 20

$\dot{q}$, Btu/ft^2-sec

(c) Test 22. $\Lambda = 60°$.

Figure 28. Overall heating distributions in high-energy turbulent flow. $\dot{q}_{FP} = 5.8$ Btu/ft^2 – sec; $W = 0.070$ in.

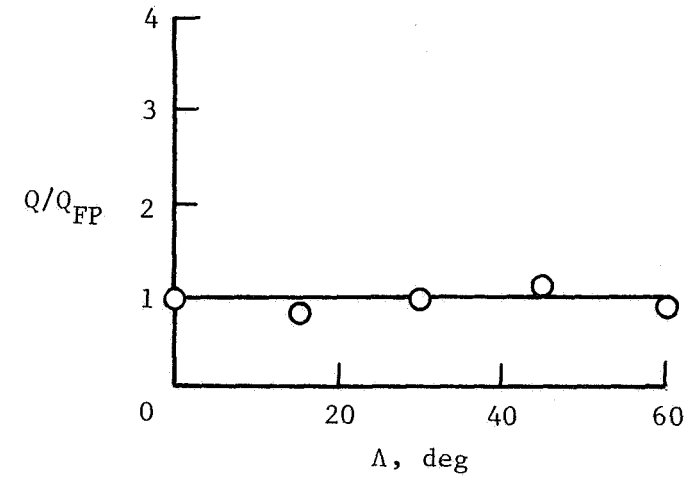

(a) Low-energy turbulent flow.

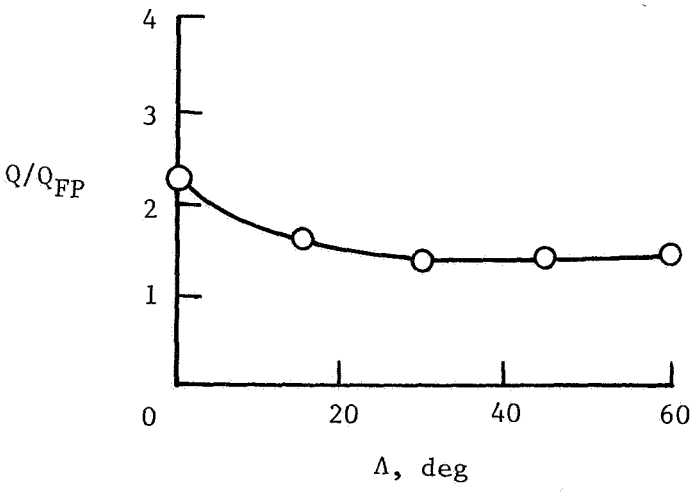

(b) High-energy turbulent flow.

Figure 29. Effect of flow angularity on total heat load in turbulent flow. $W = 0.070$ in.

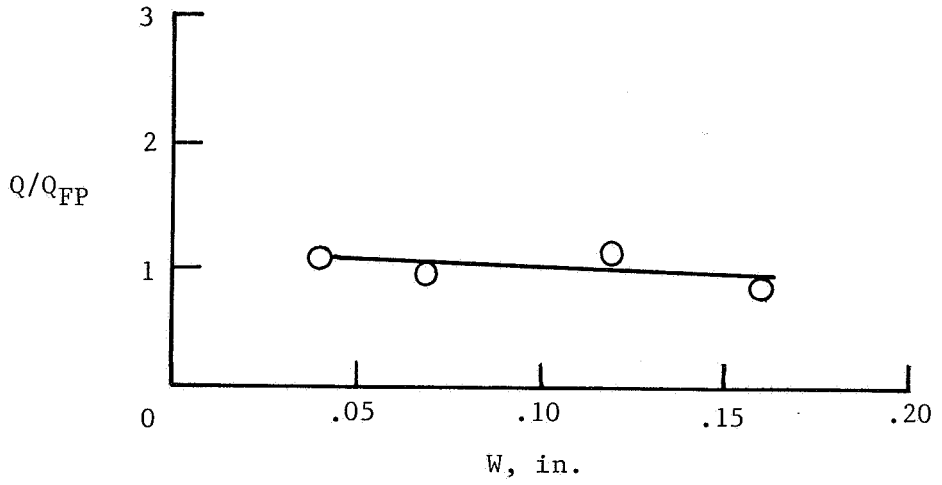

(a) Low-energy turbulent flow.

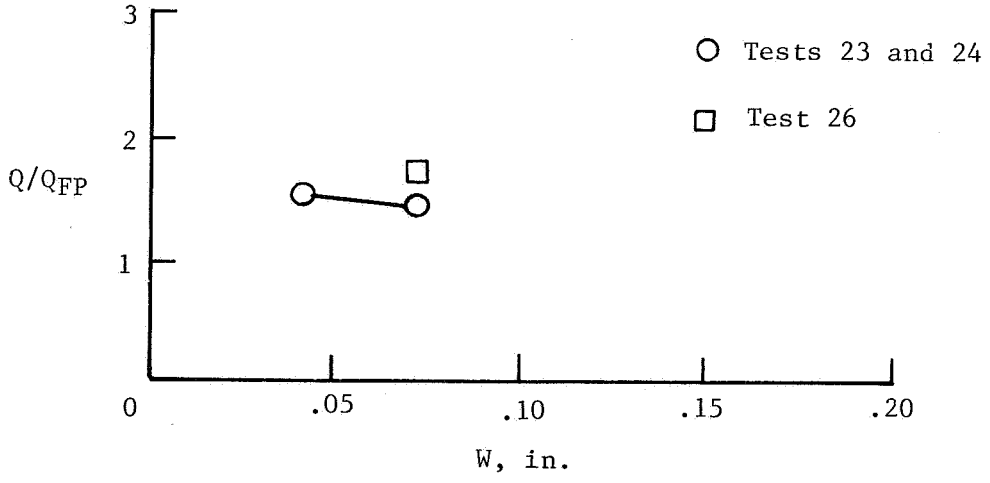

(b) High-energy turbulent flow.

Figure 30. Effect of gap width on total heat load in turbulent flow. $\Lambda = 45°$.

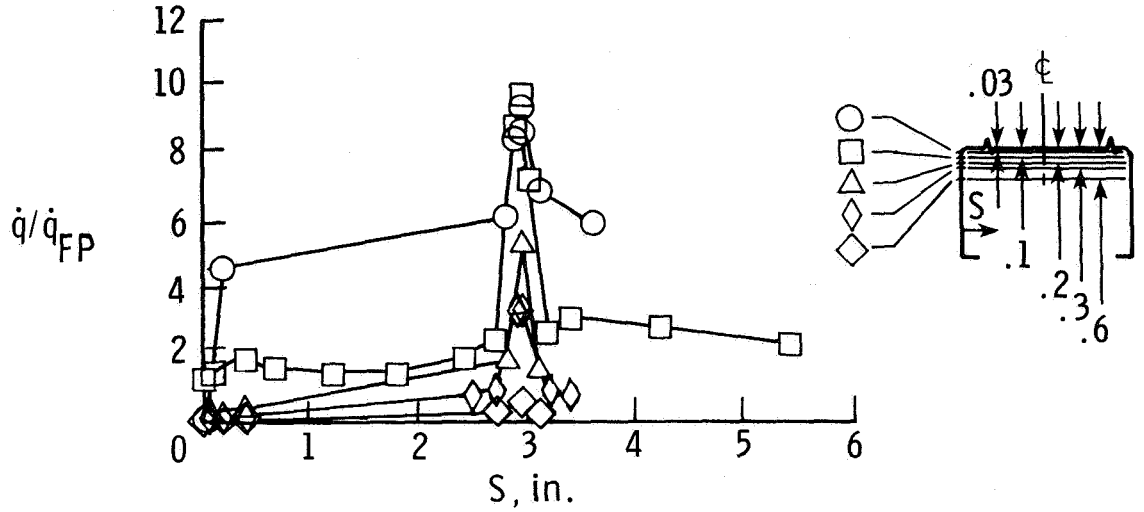

(a) Heating distribution across front face (side 1) with nominal step height of 0.035 in. Test 19.

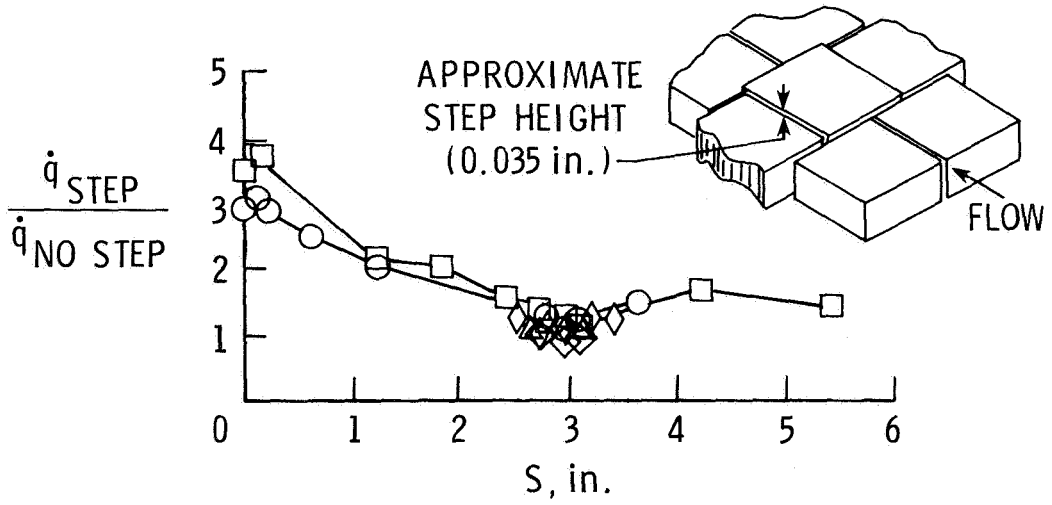

(b) Ratio of heating with step to heating with no step across side 1. Tests 19 and 17, respectively.

Figure 31. Increased heating due to raised tile. Dimensions are given in inches unless otherwise specified.

Standard Bibliographic Page

1. Report No.	2. Government Accession No.	3. Recipient's Catalog No.
NASA TP-2307		

4. Title and Subtitle	5. Report Date
Experimental Aerodynamic Heating to Simulated Space Shuttle Tiles in Laminar and Turbulent Boundary Layers With Variable Flow Angles at a Nominal Mach Number of 7	August 1985
	6. Performing Organization Code: 506-51-23-03
7. Author(s): Don E. Avery	8. Performing Organization Report No.: L-15781
9. Performing Organization Name and Address: NASA Langley Research Center, Hampton, VA 23665	10. Work Unit No.
	11. Contract or Grant No.
12. Sponsoring Agency Name and Address: National Aeronautics and Space Administration, Washington, DC 20546	13. Type of Report and Period Covered: Technical Paper
	14. Sponsoring Agency Code

15. Supplementary Notes

Submitted in partial fulfillment of the requirements for the Degree of Master of Science, George Washington University, Washington, D.C., November 1983.

16. Abstract

The heat transfer to simulated Shuttle thermal protection system tiles was investigated experimentally by using a highly instrumented metallic thin-wall tile arranged with other metal tiles in a staggered tile array. Cold-wall heating-rate data for laminar and turbulent flow were obtained in the Langley 8-Foot High-Temperature Tunnel at a nominal Mach number of 7, a nominal total temperature of 3300°R, a free-stream unit Reynolds number from 3.4×10^5 to 2.2×10^6 per foot, and a free-stream dynamic pressure from 2.1 to 9.0 psia. Experimental data are presented to illustrate the effects of flow angularity and gap width on both local peak heating and overall heating loads. For the conditions of the present study, the results show that localized and total heating are sensitive to changes in flow angle only for the test conditions of turbulent boundary-layer flow with high kinetic energy and that a flow angle from 30° to 50° will minimize the local heating.

17. Key Words (Suggested by Authors(s))	18. Distribution Statement
Space Shuttle Hypersonic flow Thermal protection systems Reusable surface insulation Impingement heating	Unclassified—Unlimited Subject Category 34

19. Security Classif.(of this report)	20. Security Classif.(of this page)	21. No. of Pages	22. Price
Unclassified	Unclassified	48	A03

For sale by the National Technical Information Service, Springfield, Virginia 22161

NASA-Langley, 1985